Spatiotemporally resolved transcriptome atlas of developing mouse placenta reveals mechanisms of embryonic lethality

Yuting Fu[1,2,3,4,13], Xiaoqi Zeng[5,6,7,13], Yifang Liu[1,2,3,4,13], Shikai Jia[1,2,3,4,13], Yujia Jiang[5,6,8,13], Jia Ping Tan[1,2,3,4], Yue Yuan[5,6], Tianchang Xia[1,2,3,4], Yun Mei[1,2,3,4], Shan Wen[1,2,3,4], Xiaojing Liu[1,2,3,4], Yue You[9,10], Weike Pei[1,11], Chengshuo Yang[2,12], Sida Shao[2,12], Saifeng Cheng[1,3], Luyi Tian[9,10], Longqi Liu[5]*, Xiaoyu Wei[5]*, Xiaodong Liu[1,2,3,4]*

[1]School of Life Sciences, Westlake University, Hangzhou, Zhejiang, China
[2]Research Center for Industries of the Future, Westlake University, Hangzhou, China
[3]Westlake Laboratory of Life Sciences and Biomedicine, Hangzhou, Zhejiang, China
[4]Westlake Institute for Advanced Study, Hangzhou, Zhejiang, China
[5]BGI Research, Hangzhou 310030, China
[6]BGI Research, Shenzhen 518083, China
[7]College of Life Sciences, University of Chinese Academy of Sciences, Beijing 100049, China
[8]Department of Biology, University of Copenhagen, 2100 Copenhagen, Denmark
[9]Guangzhou National Laboratory, Guangzhou, China
[10]GMU-GIBH Joint School of Life Sciences, Guangzhou Medical University, Guangzhou, Guangdong, China
[11]Center for Infectious Disease Research, Westlake Laboratory of Life Sciences and Biomedicine, Hangzhou 310024, Zhejiang, China
[12]Department of Chemistry, School of Science, Westlake University, Hangzhou, China
[13]These authors contributed equally
*Correspondence: Longqi Liu (L.L.) liulongqi@genomics.cn; Xiaoyu Wei (X.W.); weixiaoyu@genomics.cn; Xiaodong Liu (X.L.) liuxiaodong@westlake.edu.cn

Summary

Proper placentation is essential for embryonic growth and viability, yet the spatial organization and interactions of placental cell types remain incompletely understood. Here, we present a spatiotemporal transcriptomic atlas of the mouse placenta (STAMP) from embryonic days 9.5 to 18.5 at single-cell resolution. This atlas delineates major placental cell types and developmental trajectories. We observed labyrinth region expansion through branching morphogenesis, with trophoblast progenitor cells declining and terminally differentiated trophoblast cells increasing from E12.5 onward, and glycogen cells (GCs) transitioned from the junctional zone (JZ) to the maternal decidua. Furthermore, we found two novel GC subclusters with distinct spatial distributions and molecular features. Analysis of defective placentas revealed an increased number of GCs and altered macrophage distribution in the labyrinth layer. Transmission electron microscopy and glycogen content examination confirmed sluggish glycogen breakdown, while macrophage accumulation correlated with tissue remodeling and immune responses. Our spatial transcriptomic analysis elucidates mechanisms underlying placental abnormalities and embryonic lethality. This atlas enhances understanding of mouse placental development, aids in identifying developmental defects and pathogenic causes in dysfunctional placentas, and provides valuable insights for optimizing *in vitro* embryo culture conditions.

Introduction

The placenta, a sophisticated and unique organ, plays an indispensable role during mammalian pregnancy. It not only serves as a physical barrier between maternal blood and the fetus, but also performs crucial functions such as delivering oxygen and nutrients to the fetus and removing waste.[1,2,3] A dysfunctional placenta is often linked to various pregnancy-related disorders, including miscarriage, preeclampsia, and fetal intrauterine growth restriction.[4,5,6]

The morphological and functional similarities between human and mouse placentas make the mouse a key model for studying the impact of placenta development on pregnancy and the mechanisms underlying placental dysfunction.[7,8] After mouse gastrulation, the chorioallantoic fusion initiates the formation of the labyrinth around embryonic day (E) 9.5. This complex structure allows maternal and fetal blood to circulate closely yet separately, optimizing nutrient and oxygen transport essential for fetal development.[9] Defects in labyrinth formation can frequently cause developmental failures and growth deficits, as this structure is critical for

nutrient transfer from mid-gestation onwards.[10,11] As placental function gradually matures, nutritional support for the developing fetus shifts from histotrophic nutrition (i.e., phagocytic uptake of maternal secretions by embryonic cells) to hematogenous nutrition (i.e., countercurrent exchange of vascular-borne nutrients along concentration gradients).[12] This conversion is essential to meet the nutrient needs of the rapidly growing embryo.[13] Thus, gaining a deep understanding of placental function is crucial for supporting embryo growth. This is particularly important for *in vitro* culturing of embryos and embryo models, where the placenta can facilitate late-stage embryonic development.[14,15]

Recent efforts have focused on studying loss of gene function in mice using CRISPR-Cas9 technology for rapid mutation induction, primarily to understand the functional consequences of these gene mutants during embryonic development or adulthood. However, it has been shown that 68% of mouse knockout lines that are lethal at or after mid-gestation exhibit placental dysmorphologies, with early embryonic deaths between E9.5 and E14.5 almost invariably associated with significant placental malformations.[10] These placental defects have been shown to correlate strongly with abnormal brain, heart and vascular development.[16] Therefore, understanding the cellular and molecular mechanisms of placental abnormalities is crucial for comprehending how this vital organ contributes to normal development.

Previous studies have identified cell types comprising trophoblast-derived lineages of mouse placentas at various developmental stages (from E7.5 to E14.5) using single cell/nucleus RNA-sequencing.[17,18] However, a comprehensive understanding of spatial cell type organization, cell-cell interactions, and gene expression patterns along the maternal-fetal axis during placentation is still lacking. Recent developments in spatial transcriptomic technologies can capture transcriptional profiles while maintaining the spatial context of cells, providing deep insights into the *in situ* molecular dynamics of cell types within different organs.[19,20,21] We systematically compared several sequencing-based methods and found that Stereo-seq has exceptional performance in sensitivity and resolution,[22] allowing for the effective identification of cell types and states at single-cell resolution.[23] Here, we reconstructed a spatiotemporal atlas of mouse placentation from E9.5 to E18.5 using Stereo-seq. The data is accessible via an interactive data portal named Spatiotemporal Transcriptomic Atlas of Mouse Placenta (STAMP) (https://db.cngb.org/stomics/stamp/).

This study spatially resolved major placental cell types and developmental trajectories. From E12.5 onwards, trophoblast progenitor cells declined while terminally differentiated trophoblast cells increased, and glycogen cells (GCs) transitioned from the junctional zone (JZ) to the maternal decidua. Spatially resolved transcriptomic profiling identified two previously

unreported GC subclusters and detailed their lineage trajectories. In defective placentas, we observed an increased number of GCs and altered macrophage distribution in the labyrinth layer, elucidating the mechanisms behind placental abnormalities and embryonic lethality. Our atlas enhances understanding of mouse placental development, identifies defects in dysfunctional placentas, and provides insights for optimizing *in vitro* embryo culture conditions.

Results

Single-cell spatiotemporal transcriptomic atlas of the developing mouse placenta

To gain a comprehensive understanding of cell fate transitions and specifications at spatial and temporal resolution during placentation, we profiled 9 mouse placentas at developmental stages ranging from E9.5 to E18.5 using Stereo-seq and snRNA-seq (Figure 1A, S1A, S1B, and S1C). We conducted a series of data quality control measures for downstream analyses (see Methods) and identified 35 distinct clusters. These clusters can be broadly classified based on feature gene expression into trophoblast cells (14 subclusters), stromal cells (4 subclusters), immune cells (7 subclusters), endothelial cells (EC) (4 subclusters) and other cell types from fetal and maternal tissues (Figure 1B and S1D).[17,18,24,25,26] We validated our findings by cross-referencing them with existing placental datasets from other studies. The results demonstrated strong consistency, with substantial overlaps with published datasets (Figure S1E).

We used DNA staining and the watershed algorithm[23] to achieve single-cell resolution, extracting transcripts within defined nuclear and cytoplasmic boundaries. Spatially constrained clustering (SCC) identified clusters corresponding to anatomical regions like the labyrinth, junctional zone (JZ), maternal decidua, and myometrium (Figure S2A). Using the snRNA-seq data as a reference, the TACCO (v0.3.0) framework annotated the Stereo-seq data,[27] assigning each cell the most probable cell type (Figure S2B). This allowed us to map the spatial and temporal transitions of all cell types within the placenta from E9.5 to E18.5. The data are accessible on our interactive data portal, the Spatiotemporal Transcriptomic Atlas of Mouse Placenta (STAMP) (https://db.cngb.org/stomics/stamp/) (Figure 1C, 1D, S2C and S2D).

For the first time, we identified diverse spatial distributions and fate dynamics of cell types across various regions of the developing placentas, elucidating their region-specific functions

and implications for placental biology. We observed that the labyrinth region expands through branching morphogenesis, creating intricate vascular spaces for maternal-fetal blood circulation.[9] Additionally, the proportion of trophoblast progenitor cells in the labyrinth region declines from E9.5, while terminally differentiated trophoblast cells increase after E12.5, indicating the development of a mature mouse placenta (Figure 1C and 1D). Concurrently, spongiotrophoblast cells (SpT) and glycogen cells (GC) begin to mature from E12.5 onwards. Notably, we observed a spatial transition of GCs from the junctional zone (JZ) to the maternal decidua region, which initially appear in the JZ at E12.5, peak at E14.5, and then gradually decline. Concurrently, GCs in the decidua start emerging at E13.5 and steadily increase until E18.5 (Figure 1C and 1D). This observed pattern broadly corresponds to previous immunostaining results for protocadherin 12 (PCDH12), a marker specifically expressed in GCs.[28,29] In contrast, other cell types, including endothelial cells, immune cells, and stromal cells were primarily localized in the maternal decidua region (Figure 1C and 1D).

Importantly, by leveraging our spatial transcriptomic dataset, we were able to identify both multinucleated syncytiotrophoblast cells and trophoblast giant cells (TGCs) at consecutive stages *in situ* (Figure 1C and 1D), which could not be achieved by previously reported single cell RNA-seq or single nuclei RNA-seq studies.[17,18]

Interestingly, we visualized the spatial dynamics of two previously reported decidual stromal cells (DSCs), angiogenic DSC and nourishing DSC with distinct molecular signatures and functions within the maternal decidual region.[24] From E9.5, the localization of angiogenic DSCs gradually shifts towards the top of the decidua, closer to the myometrium. This positioning promotes angiogenesis, with their numbers increasing until stabilizing after E14.5. Conversely, the population of nourishing DSCs, which are involved in cellular energy homeostasis and hormone catabolic processes, gradually diminishes.[24,30] Their distribution shifts towards the fetal side of the placenta over time (Figure 1C and 1D).

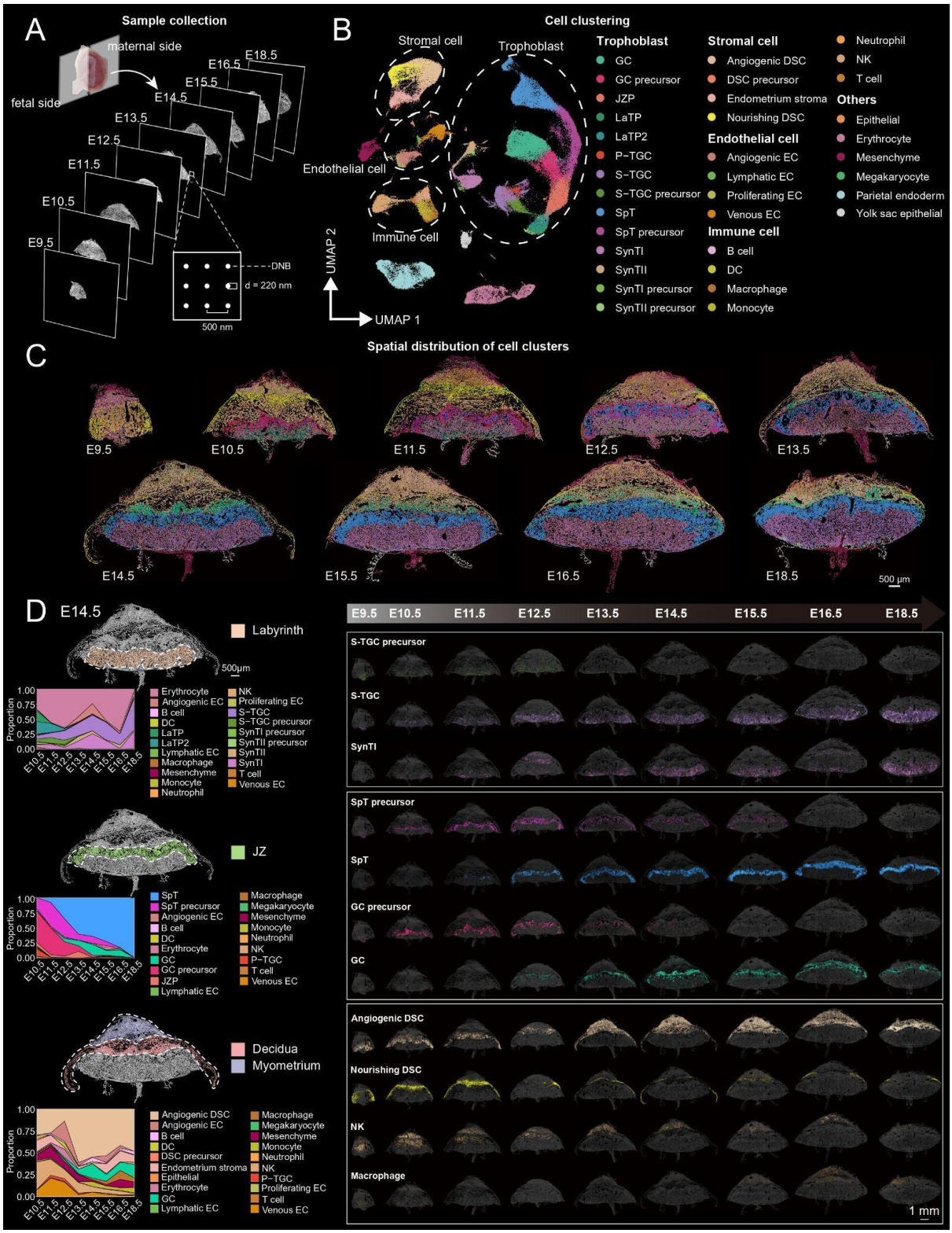
A
Sample collection
maternal side
fetal side
E9.5
E10.5
E11.5
E12.5
E13.5
E14.5
E15.5
E16.5
E18.5
DNB
d = 220 nm
500 nm
B
Cell clustering
Stromal cell
Trophoblast
Endothelial cell
Immune cell
UMAP 2
UMAP 1
Trophoblast
GC
GC precursor
JZP
LaTP
LaTP2
P−TGC
S−TGC
S−TGC precursor
SpT
SpT precursor
SynTI
SynTII
SynTI precursor
SynTII precursor
Stromal cell
Angiogenic DSC
DSC precursor
Endometrium stroma
Nourishing DSC
Endothelial cell
Angiogenic EC
Lymphatic EC
Proliferating EC
Venous EC
Immune cell
B cell
DC
Macrophage
Monocyte
Neutrophil
NK
T cell
Others
Epithelial
Erythrocyte
Mesenchyme
Megakaryocyte
Parietal endoderm
Yolk sac epithelial
C
Spatial distribution of cell clusters
E9.5
E10.5
E11.5
E12.5
E13.5
E14.5
E15.5
E16.5
E18.5
500 μm
D
E14.5
Labyrinth
500μm
Proportion
JZ
Decidua
Myometrium
E9.5 E10.5 E11.5 E12.5 E13.5 E14.5 E15.5 E16.5 E18.5
S-TGC precursor
S-TGC
SynTI
SpT precursor
SpT
GC precursor
GC
Angiogenic DSC
Nourishing DSC
NK
Macrophage
1 mm

Figure 1. Single-cell spatiotemporal transcriptomic atlas of the developing mouse placenta

(A) Schematic illustration of the placenta samples collected for spatial transcriptomics profiling.
(B) Uniform manifold approximation and projection (UMAP) of snRNA-seq clustering showing 35 cell types. GC, glycogen trophoblast cell; JZP, junctional zone progenitor; LaTP, labyrinth trophoblast progenitor; P-TGC, parietal trophoblast giant cell; S-TGC, sinusoid trophoblast giant cell; SpT, spongiotrophoblast cell; SynT, syncytiotrophoblast cell; DSC, decidual stromal cell; EC, endothelial cell; DC, dendritic cell; NK, natural killer cell.
(C) Spatial visualization of all cell distributions within placentas at different developmental stages from E9.5 to E18.5 using Stereo-seq data. Cells are colored by their annotations. Scale bars, 500 μm.
(D) Cell type distribution and quantification in placenta sections from E9.5 to E18.5. Anatomical regions (left) were identified as Labyrinth zone, Junctional zone (JZ), Maternal decidua, and Myometrium. Regions are colored based on anatomical region annotations. Cells are colored based on cell type annotations. Stacked area plots showing cell type proportions in the corresponding regions. Scale bars, 500 μm.

Identification and characterization of glycogen cells with distinct spatial distributions and molecular features

Next, we specifically investigated the spatiotemporal development of trophoblast cells which are the major cell types within the placenta. We performed a reclustering analysis of snRNA-seq data and identified two distinct GC subclusters (Figure 2A). We then examined the spatial distributions of these two GC subclusters using Stereo-seq data. Interestingly, the analysis allowed us to use the spatial information to distinguish these two GC subclusters, with one GC subcluster (GC-1) was mainly located within the JZ, while another GC subcluster (GC-2) was restricted to the maternal decidua (Figure 2B).

To elucidate the molecular differences between these previously unidentified GCs, we conducted a differential gene expression analysis (Figure 2C and S3A). Aldehyde dehydrogenase family1, member A3 (*Aldh1a3*), a marker of glycogen trophoblast cells and their precursors,[31] showed elevated expression in GC-1. While GC-2 highly expressed prolactin family 7, subfamily B, member 1 (*Prl7b1*), which is detected in maternal decidua and shows expression patterns overlapping with *Pcdh12* by *in situ* hybridization.[32] The spatial expression patterns of *Aldh1a3* and *Prl7b1* align with the spatial distributions of GC-1 and GC-

2, respectively (Figure S3B). Additionally, enriched gene ontology (GO) biological processes revealed functional disparities between the two GC subclusters. Genes highly expressed in GC-1 were implicated in processes such as chromatin remodeling, regulation of GTPase activity, and small GTPase-mediated signal transduction. Conversely, genes upregulated in GC-2 were associated with processes such as epithelial cell migration, artery morphogenesis, artery development, and regulation of vasculature development (Figure 2C). The enriched gene ontology (GO) biological processes confirmed that GCs invade the maternal decidua and interact with spiral arteries to deliver maternal blood to the placenta.[29,33,34] In addition, the shared genes between GC-1 and GC-2 were enriched in glycogen metabolism processes, indicating both subclusters' roles in glycogen metabolism (Figure 2C).

To uncover the essential transcription factors (TFs) governing GC fate transitions and functions, we performed SCENIC analysis to evaluate TF expression and motif enrichment near promoters of co-expressed genes, revealing transcriptional network dynamics. By analyzing the differentially expressed genes (DEGs) of GC-1 and GC-2, we identified regulons with differential activity, including both known TFs such as *Tfap2c*, *Tcf12*, *Prdm1*, and *Fosl2*, [35,36,37,38] and novel TFs like *Nfib*, *Elf4*, *Etv6*, *Anxa11* in GC-1, and *Creb5* in GC-2. The regulon was validated by gene module scores from Stereo-seq data, showing consistent spatial distributions of the regulons on the E14.5 placenta section (Figure 2D and S3C). To further investigate the functional differences between GC-1 and GC-2, we analyzed the cellular communications between the two GC subclusters and surrounding cell types using the CellChat algorithm.[39] The analysis revealed distinct communication networks between GC-1 and GC-2 (Figure S3D and S3E). Notably, GC-2 interactions featured ligand-receptor pairs such as *Sema3e-Plxnd1*, emphasizing its regulatory role in angiogenesis. Additionally, ligand-receptor pairs including *Lgals9-Ptprc*, *Lgals9-Ighm*, *Lgals9-Havcr2*, and *Lgals9-Cd44* indicated potential immunomodulatory effects. We also observed predominant expression of *Ccl27a* signals in GC-2, which are involved in immune cell recruitment (Figure S3E). Both GC-1 and GC-2 demonstrated the capacity to secrete growth factors (Figure S3D and S3E).

Next, we performed a cellular temporal trajectory analysis of the GC lineage. The spatial position changes for the two GC subclusters over time indicated that GC-1 initially appeared in the junctional zone (JZ), exhibiting a brief increase in number before gradually declining (Figure 2E and S3F). In contrast, GC-2 emerged after E13.5, being exclusively distributed in the maternal decidua, with numbers steadily increasing until E18.5 (Figure 2E and S3F). The total number of GCs increased from E12.5 to E16.5, followed by a significant decrease by E18.5 (Figure 2E and S3F), consistent with previous findings of extensive GCs lysis during the perinatal period.[29,40] Despite their crucial metabolic role in the placenta,[41] the detailed

developmental trajectory of GCs has not been previously reported. We performed cellular trajectory reconstruction of trophoblast cells using Monocle3[42] and CytoTRACE,[43] revealing several main developmental trajectories (Figure S4A).[17] To precisely understand the GC lineage trajectory, we extracted junctional zone progenitor (JZP), GC precursor, and two GC subclusters for further temporal analysis. This revealed a temporal relationship between the two GC subclusters, illustrating the lineage transition along the JZP-GC precursor-GC-1-GC-2 pattern (Figure 2F, 2G, 2H, and 2I).

In summary, by utilizing spatially resolved transcriptomic profiling, we were able to identify two GC subclusters with distinct spatial distributions and molecular features, and delineate their dynamic cell state transitions and regulatory network.

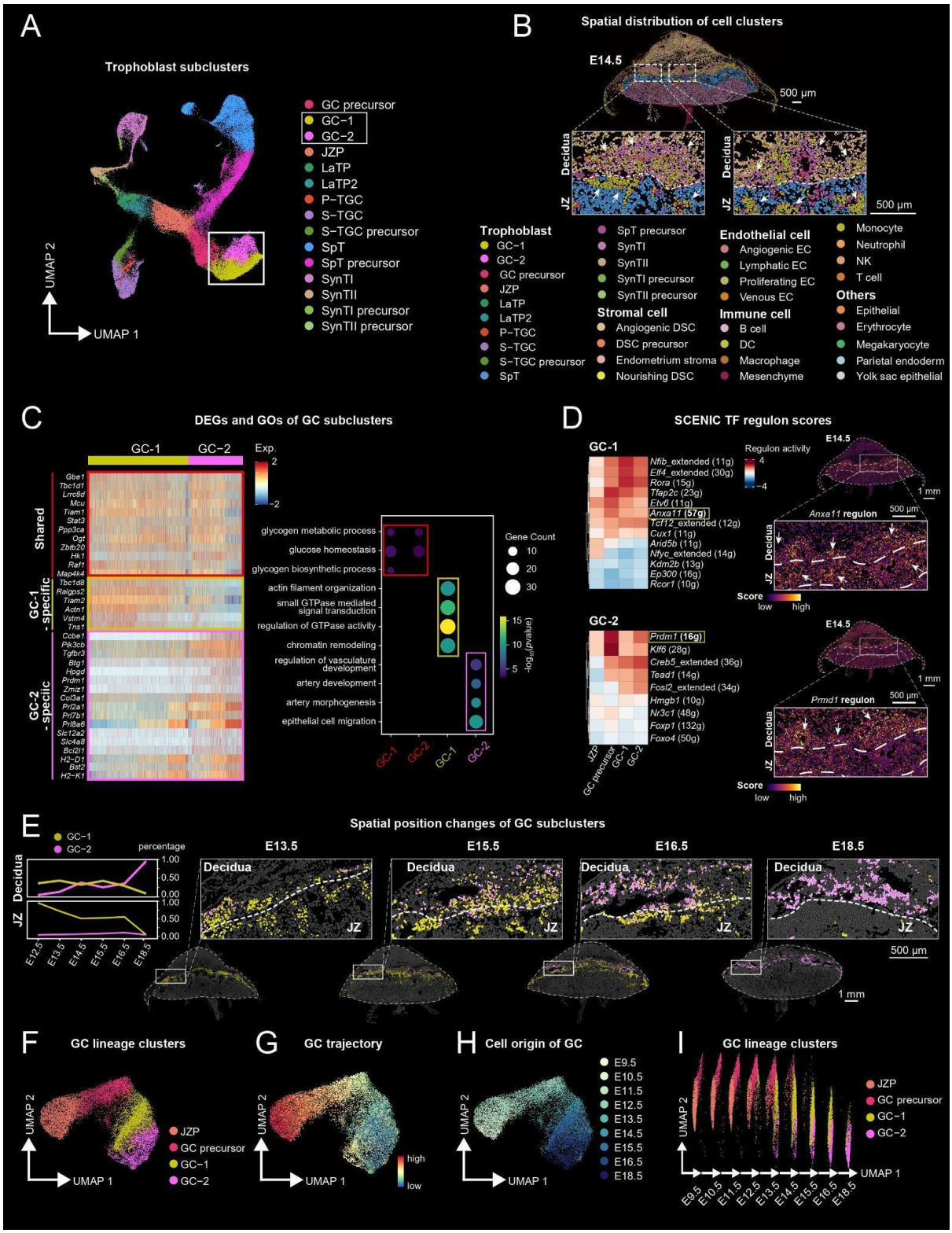
A
Trophoblast subclusters
GC precursor
GC−1
GC−2
JZP
LaTP
LaTP2
P−TGC
S−TGC
S−TGC precursor
SpT
SpT precursor
SynTI
SynTII
SynTI precursor
SynTII precursor
UMAP 2
UMAP 1
B
Spatial distribution of cell clusters
E14.5
500 μm
Decidua
JZ
Trophoblast
GC−1
GC−2
GC precursor
JZP
LaTP
LaTP2
P−TGC
S−TGC
S−TGC precursor
SpT
SpT precursor
SynTI
SynTII
SynTI precursor
SynTII precursor
Stromal cell
Angiogenic DSC
DSC precursor
Endometrium stroma
Nourishing DSC
Endothelial cell
Angiogenic EC
Lymphatic EC
Proliferating EC
Venous EC
Immune cell
B cell
DC
Macrophage
Mesenchyme
Monocyte
Neutrophil
NK
T cell
Others
Epithelial
Erythrocyte
Megakaryocyte
Parietal endoderm
Yolk sac epithelial
C
DEGs and GOs of GC subclusters
GC-1
GC−2
Exp.
Shared
GC-1 - specific
GC-2 - specific
glycogen metabolic process
glucose homeostasis
glycogen biosynthetic process
actin filament organization
small GTPase mediated signal transduction
regulation of GTPase activity
chromatin remodeling
regulation of vasculature development
artery development
artery morphogenesis
epithelial cell migration
Gene Count
D
SCENIC TF regulon scores
GC-1
Nfib_extended (11g)
Elf4_extended (30g)
Rora (15g)
Tfap2c (23g)
Etv6 (11g)
Anxa11 (67g)
Tcf12_extended (12g)
Cux1 (11g)
Arid5b (11g)
Nfyc_extended (14g)
Kdm2b (13g)
Ep300 (16g)
Rcor1 (10g)
Regulon activity
Anxa11 regulon
GC-2
Prdm1 (16g)
Klf6 (28g)
Creb5_extended (36g)
Tead1 (14g)
Fosl2_extended (34g)
Hmgb1 (10g)
Nr3c1 (48g)
Foxp1 (132g)
Foxo4 (50g)
Prmd1 regulon
Score
low
high
1 mm
500 μm
E
Spatial position changes of GC subclusters
percentage
E13.5
E15.5
E16.5
E18.5
F
GC lineage clusters
G
GC trajectory
H
Cell origin of GC
E9.5
E10.5
E11.5
E12.5
E13.5
E14.5
E15.5
E16.5
E18.5
I
GC lineage clusters

Figure 2. Identification of Glycogen cell (GC) subclusters with distinct spatial distribution and molecular features

(A) UMAP visualization showing the reclustering of trophoblast cells.

(B) Spatial visualization of all cell distributions in the E14.5 placenta section. Two magnified fields of view highlight the distinct spatial distribution of the two GC subclusters. Scale bars, 500 μm.

(C) Heatmap (left) showing the DEGs of GC subclusters, with significantly enriched GOs shown by bubble plot (right). Shared genes and GOs are outlined in red, GC-1-specific genes and GOs are outlined in yellow, and GC-2-specific genes and GOs are outlined in pink.

(D) Heatmap (left) showing the SCENIC transcription factor (TF) regulon scores in GC-1 and GC-2 based on regulon activity. Spatial visualization of selected regulons, *Anxa11* and *Prmd1*, are shown respectively in the E14.5 placenta section (right).

(E) Line chart (left) showing the percentage of the two GC subclusters in the maternal decidua and JZ region from E12.5 to E18.5. The spatial visualization of the two GC subclusters at E13.5, E15.5, E16.5 and E18.5 is shown on the right. Cells are colored by their annotations. Scale bars, 500 μm.

(F) UMAP visualization showing cell types across GC differentiation, including junctional zone progenitor (JZP), GC precursor, and two GC subclusters. Cells are colored by cell type annotation.

(G) Pseudotime trajectory of cell types across GC differentiation, analyzed using Monocle3 and CytoTRACE. Cells are colored by pseudotime.

(H) UMAP visualization showing the origin of GC based on the time point.

(I) UMAP visualization of cell types across GC differentiation. Cells are colored by cell type annotation.

Cellular trajectory analyses revealed genes that affect placenta development

To study the placental development in mouse mutants with impaired placental function, we first compiled a list of mouse mutant lines previously associated with embryonic lethality and potentially linked to impaired placental development. This list comprised 103 mouse knockout lines sourced from the Deciphering the Mechanisms of Developmental Disorders program (https://dmdd.org.uk),[10] along with an additional 48 mouse mutant lines, totaling 151 lines. We categorized these genes based on the timing of lethality and examined previous research findings for indications of placental development defects (Table 1). Next, through trajectory analysis of trophoblast cells using Monocle3[42] and CytoTRACE,[43] we delineated five principal

trophoblast cell lineage progression trajectories, including the GC lineage (Figure S4A and S4B). Subsequently, we isolated genes temporally expressed along pseudotime within each trajectory, indicating changes in gene expression throughout the developmental process. These genes may encompass those driving or determining crucial points in placental development (Figure S4C).[44] Interestingly, we identified a gene named *Ano6*, which plays a significant role in GC lineage development and has been implicated in influencing placental development (Figure 3A, 3B, S5A, and S5B). Furthermore, our differential gene expression analysis suggested that *Ano6* is specifically expressed in GCs (Figure 3C). This observation was further supported by RIBOmap analysis,[45] which provides spatially resolved measurements of *Ano6* protein synthesis predominantly within the JZ region at E13.5 (Figure 3D). Next, we investigated the expression patterns of the *Ano6* gene in both fetal and placental tissues throughout development. Our analysis revealed a notable increase in *Ano6* expression within the developing placenta from E8.5 to E18.5 (Figure S6A). This dynamic expression pattern underscores the potential importance of *Ano6* in placental development across various stages.

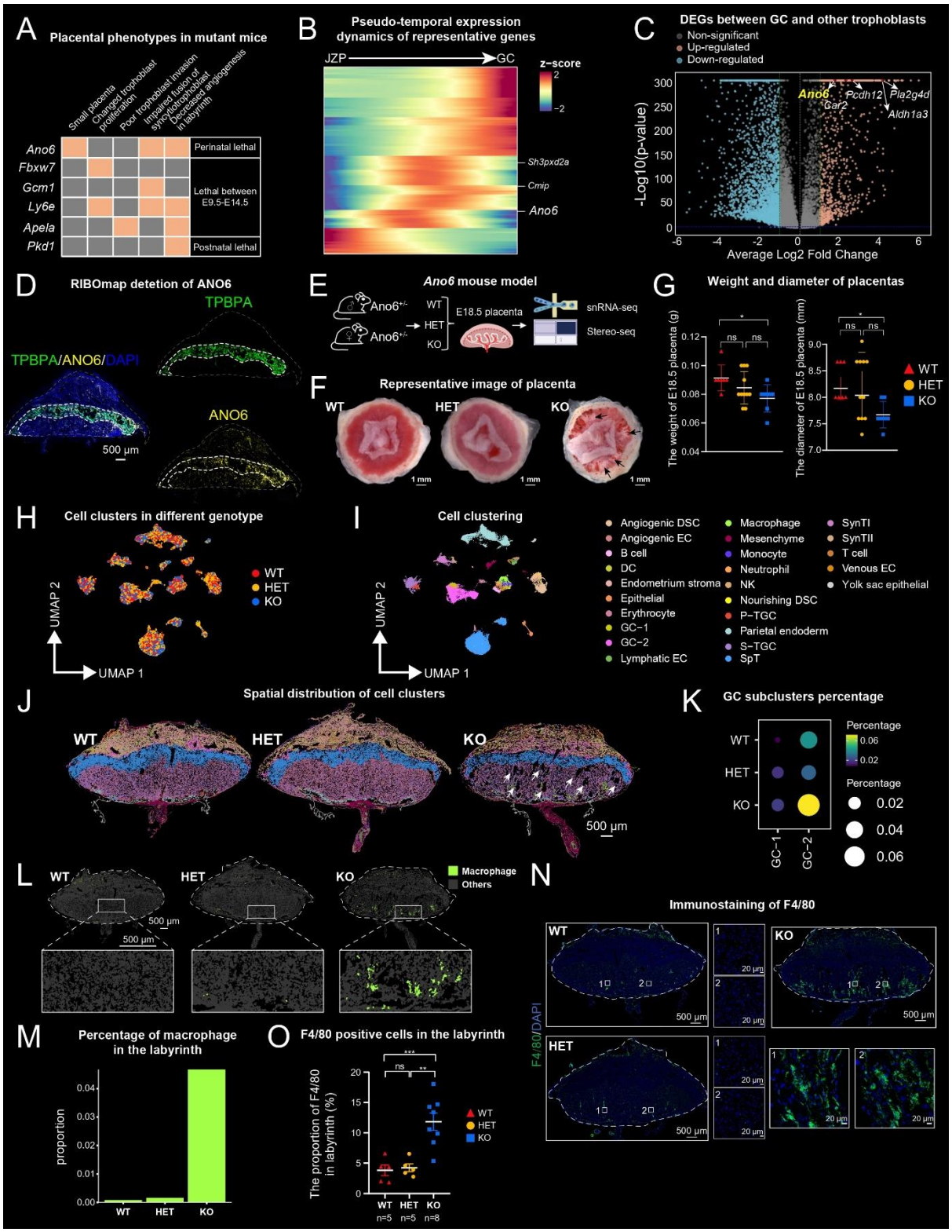
A
Placental phenotypes in mutant mice
Small placenta
Changed trophoblast proliferation
Poor trophoblast invasion
Impaired fusion of syncytiotrophoblast
Decreased angiogenesis in labyrinth
Ano6
Fbxw7
Gcm1
Ly6e
Apela
Pkd1
Perinatal lethal
Lethal between E9.5-E14.5
Postnatal lethal
B
Pseudo-temporal expression dynamics of representative genes
JZP
GC
z-score
Sh3pxd2a
Cmip
Ano6
C
DEGs between GC and other trophoblasts
Non-significant
Up-regulated
Down-regulated
Ano6
Pcdh12
Pla2g4d
Car2
Aldh1a3
-Log10(p-value)
Average Log2 Fold Change
D
RIBOmap detetion of ANO6
TPBPA
TPBPA/ANO6/DAPI
ANO6
500 μm
E
Ano6 mouse model
Ano6+/-
WT
HET
KO
E18.5 placenta
snRNA-seq
Stereo-seq
F
Representative image of placenta
WT
HET
KO
1 mm
G
Weight and diameter of placentas
The weight of E18.5 placenta (g)
The diameter of E18.5 placenta (mm)
ns
WT
HET
KO
H
Cell clusters in different genotype
UMAP 2
UMAP 1
WT
HET
KO
I
Cell clustering
Angiogenic DSC
Angiogenic EC
B cell
DC
Endometrium stroma
Epithelial
Erythrocyte
GC-1
GC-2
Lymphatic EC
Macrophage
Mesenchyme
Monocyte
Neutrophil
NK
Nourishing DSC
P-TGC
Parietal endoderm
S-TGC
SpT
SynTI
SynTII
T cell
Venous EC
Yolk sac epithelial
J
Spatial distribution of cell clusters
WT
HET
KO
500 μm
K
GC subclusters percentage
Percentage
0.06
0.02
GC-1
GC-2
L
WT
HET
KO
Macrophage
Others
500 μm
M
Percentage of macrophage in the labyrinth
proportion
N
Immunostaining of F4/80
F4/80/DAPI
20 μm
O
F4/80 positive cells in the labyrinth
The proportion of F4/80 in labyrinth (%)
n=5
n=5
n=8

Figure 3. Spatial transcriptomic analysis of the placental defects in embryonic-lethal mouse mutant

(A) Representation of the curated list of embryonic lethal mouse mutant genes (orange denotes abnormality detected). The selected mutant genes are categorized by lethality stage and marked with corresponding placental phenotypes.

(B) Pseudo-temporal expression dynamics of specific representative genes along the GC developmental trajectory.

(C) Volcano plot of differentially expressed genes (DEGs) identified between GC and other trophoblast cells. The orange dots denote up-regulated gene expression, the blue dots denote down-regulated gene expression, and the gray dots denote gene expression without marked differences. Several up-regulated genes in GC related to embryonic lethality are highlighted.

(D) Detection of *Ano6* and *Tpbpa* protein synthesis by RIBOmap[45] in E13.5 placenta sections. Dotted lines encircle the same region. Scale bars, 500 μm.

(E) Schematic illustration of the experimental design.

(F) Representative images of placentas from WT, HET, and KO mice at embryonic day 18.5 (E18.5). Black arrows point to the phenotypic defects in the KO placenta.

(G) Quantification of the weight and diameter of the WT, HET, and KO placenta. WT (n=7), HET (n=11), KO (n=7). One-way analysis of variance (ANOVA). *$p < 0.05$. All data represent means ± SEM.

(H) UMAP representation of all cell types in E18.5 WT, HET, and KO placentas.

(I) UMAP visualization of snRNA-seq clustering showing the 25 cell types in E18.5 WT, HET, and KO placenta samples.

(J) Spatial visualization of all cell distributions in Stereo-seq data. Cells are colored by their annotations. Scale bars, 500 μm.

(K) Bubble plot showing the percentage of GC subclusters in E18.5 WT, HET, and KO placentas.

(L) Spatial visualization of macrophages in E18.5 WT, HET, and KO placentas. Cells are colored by their annotations. Scale bars, 500 μm.

(M) Bar plot showing the percentage of macrophages in the labyrinth of E18.5 WT, HET, and KO placentas.

(N) F4/80 immunofluorescence staining of E18.5 WT, HET, and KO placentas. Cross sections of the entire placentas and enlarged views are shown, respectively. Scale bars, 500 μm (overall shape) and 20 μm (high-magnification view).

(O) The proportion of F4/80-positive cells in the labyrinth is quantified in WT and KO placentas. WT (n=5), HET (n=5), and KO (n=8). One-way analysis of variance (ANOVA). ***p* < 0.01, ****p* < 0.001. All data represent means ± SEM.

Spatial transcriptomic analysis of the placental defects in embryonic-lethal mouse mutant

To investigate placental defects in embryonic-lethal mice, we used a knockout strategy targeting *Ano6* by deleting exon 3 of the *Ano6*-208 transcript, resulting in a frame-shift mutation of the *Ano6* gene (Figure S6B, S6C and S6D). Given the significant decrease in postnatal survival rate among homozygous knockout (KO) mice (3.46%), we applied a heterozygous × heterozygous breeding approach to generate *Ano6* KO mice (Figure 3E, S6E and S6F). Notably, the phenotypic differences between wildtype (WT), heterozygous (HET) and KO placentas were evident after 18 days post-fertilization (Figure S7A and S7B). For example, we observed large white plaques on the fetal side of KO placentas, suggesting defects in vascular formation (Figure 3F and S8A). KO placentas were smaller and lighter than WT and HET placentas (Figure 3G). Subsequent characterization experiments revealed that KO placentas: (1) exhibited enlarged cavities within the labyrinth layer (Figure S8A); (2) displayed a smaller labyrinth area, reduced number of cells, and lower cell density compared to WT and HET placentas (Figure S8B and S8C).

Given that defects were primarily localized in the labyrinth layer, we shifted our investigation towards examining changes in cell types within this layer, focusing specifically on two syncytiotrophoblast (SynT) cell types, SynTI and SynTII. These cells play crucial roles in separating maternal blood sinuses from fetal blood vessels.[46] To characterize these cell types, we performed immunostaining of two monocarboxylate transporter proteins, MCT1 and MCT4, which selectively label SynTI and SynTII cells. Our results revealed significant reductions in the perimeters and areas of fetal blood spaces in KO placentas, indicating a diminished maternal-fetal transport surface area (Figure S8D and S8E). Additionally, we observed decreased fetal blood vessels (labeled by CD31 expression) within the labyrinth of KO placentas, suggesting insufficient branching of fetal vessels in this region (Figure S8F and S8G).[47]

Next, to provide in-depth analysis of the molecular differences *in situ*, we performed Stereo-seq combined with snRNA-seq using wildtype (WT), heterozygous (HET), and knockout (KO) samples (Figure S9A and S9B). We spatially resolved 7 major trophoblast subclusters, 7

immune cell subclusters, 3 stromal cell subclusters, 3 endothelial subclusters, and other clusters including mesenchyme, epithelial, parietal endoderm, yolk sac epithelial, and erythrocytes (Figure 3H, 3I, 3J, and S9C). Interestingly, we observed a significant increase in the number of glycogen cells in KO placentas compared to WT and HET placentas (Figure 3K). This increased presence of glycogen cells may suggest pathological glycogen accumulation during pregnancy. Furthermore, although no difference was observed in the total number of macrophages between WT, HET, and KO placentas (Figure S9D), we found a higher number of macrophages in the labyrinth of KO placentas compared to WT or HET samples (Figure 3L, 3M, and S9E). We validated the accumulation of macrophages via immunostaining using the macrophage marker F4/80 (Figure 3N, 3O, and Figure S10).

Impaired glycogen metabolism in the defective placenta

The increased presence of glycogen cells in KO placentas was further corroborated through Periodic acid-Schiff (PAS) staining and hematoxylin and eosin (H&E) staining (Figure 4A, 4B and S11). Given that glycogen is stored in glycogen cells in mice, we visualized glycogen granules within placental glycogen cells using transmission electron microscopy (TEM, Figure 4C). Our findings revealed a significantly higher number of glycogen granules in KO placental glycogen cells compared to those in WT and HET placental glycogen cells ($p < 0.001$) (Figure 4D and 4E), suggesting impaired glycogen breakdown in KO placentas. This observation was further supported by the assessment of total placental glycogen content extracted from whole WT, HET, and KO placentas, which demonstrated a significant increase in total placental glycogen content in KO placentas compared to WT and HET placentas ($p < 0.05$) (Figure 4F). A similar trend was observed when the glycogen content was adjusted for placental weight, indicating that changes in glycogen content are not driven by alterations in placental weight (Figure 4G).

Glycogen storage in the placenta acts as an energy reserve, meeting the metabolic needs of the placenta and ensuring a consistent glucose supply to the fetus, particularly during high-demand periods in late gestation. Abnormal storage of placental glycogen is associated with maternal diabetes during pregnancy and pre-eclampsia, thereby linking placental glycogen storage and metabolism to adverse pregnancy outcomes.[41] The slow glycogen breakdown in KO placentas leads to an insufficient energy supply to the fetus during the perinatal period, which might have a contribution to perinatal lethality in mutant mice.

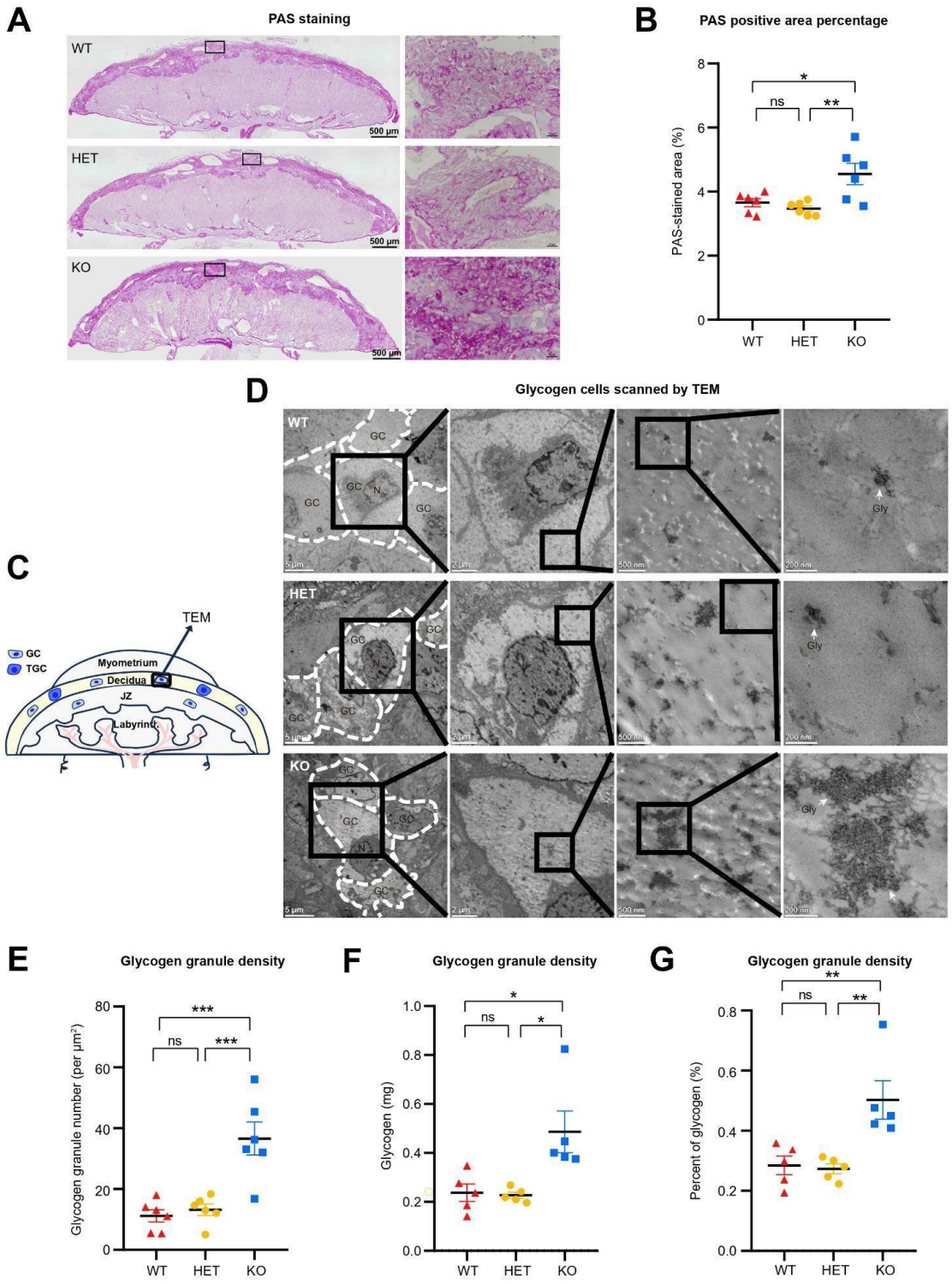

Figure 4. Impaired glycogen metabolism in the defective placenta

(A) Overall shape and high-magnification images of the PAS-stained WT, HET and KO placentas. Scale bars, 500 μm (overall shape) and 10 μm (high-magnification view).

(B) Percentage of PAS-stained positive area relative to the total tissue area analyzed using ImageJ. WT (*n*=6), HET (*n*=6), KO (*n*=6). One-way analysis of variance (ANOVA). *$p < 0.05$, **$p < 0.01$. All data represent means ± SEM.

(C) Schematic illustration of glycogen cells scanned by transmission electron microscope (TEM).

(D) Electron micrographs of WT, HET, and KO placentas at E18.5. The outline of glycogen cells is circled with white dashed lines. GC, glycogen cells; N, nucleus; Gly, glycogen granules. Scale bars, 500 μm (column 1), 200 μm (column 2), 500 nm (column 3), and 200 nm (column 4).

(E) Glycogen granule density in WT, HET, and KO placentas at E18.5. Glycogen granule number per μm^2 was calculated. WT (*n*=6), HET (*n*=6), KO (*n*=6). One-way analysis of variance (ANOVA). ***$p < 0.001$. All data represent means ± SEM.

(F) Total placental glycogen content (mg) in WT, HET, and KO placentas at E18.5. WT (*n*=6), HET (*n*=6), KO (*n*=6). One-way analysis of variance (ANOVA). *$p < 0.05$. All data represent means ± SEM.

(G) Placental glycogen expressed as a percentage of placental weight in WT, HET, and KO placentas. WT (*n*=6), HET (*n*=6), KO (*n*=6). One-way analysis of variance (ANOVA). **$p < 0.01$. All data represent means ± SEM.

Spatial accumulation of macrophages within the labyrinth is associated with immune activation and tissue repair in defective placenta

To further explore the transcriptomic differences within the labyrinth between KO and WT placentas, our differential gene expression analysis revealed 521 genes that were significantly upregulated and 253 genes that were downregulated in the labyrinth of KO placentas (adjusted $p < 0.05$ and $|\log2FC| > 1$) (Figure 5A), indicating notable alterations in gene expression patterns. Toll-like receptor genes, including *Tlr7* and *Tlr13*, showed increased expression, suggesting an activated innate immune response to infection or injury (Figure 5A and 5B).[48] Additionally, the elevated expression of chemokine ligands such as *Ccl4* and *Ccl6*,[49] along with immunomodulatory molecules like *Sirpa*, *Ccr5*, *Spp1*, *Ptafr*, and *Trem2*, indicated immune cell recruitment and an inflammatory response (Figure 5A and S12).[50,51,52,53,54,55] Moreover, the expression of solute carriers (SLCs) transmembrane transporter genes like *Slc7a2*, *Slc22a4*, and *Slc28a3* was reduced (Figure 5A and 5C). Gene Ontology (GO) enrichment analysis revealed that the upregulated genes in KO placenta were significantly enriched in processes such as tumor necrosis factor (TNF) production, leukocyte migration,

toll-like receptor signaling pathway, innate immune response, and inflammatory response (Figure 5D and S12). In contrast, the downregulated genes in KO placenta were mainly enriched in substance transport processes (Figure 5D and S13).

We then focused on the accumulated macrophages within this region and identified 140 genes that were differentially upregulated in labyrinthine macrophages (adjusted $p < 0.05$ and $|\log2FC| > 1$) (Figure 5E). These genes were significantly enriched in biological processes such as TNF production, collagen catabolic process, tissue remodeling, and leukocyte migration (Figure 5F). Notably, compared to macrophages in the maternal region, those in the labyrinth displayed heightened tissue remodeling activity, as evidenced by the increased expression of genes such as *Spp1*, *Mmp12*, *Ctss*, and *Gpnmb* (Figure 5G).[56,57,58] Moreover, the elevated expression of *Gpnmb*, *Sirpa*, and *Tyrobp* suggested that labyrinthine macrophages were in an activated immune response state, potentially participating in inflammation or tissue repair processes (Figure 5G).[59,60] Because our results indicated enlarged cavities within the labyrinth layer of KO placenta, this suggested a potential tissue damage and inflammation within this region, this could be a primary driver of macrophage migration. Importantly, the elevated expression of the macrophage surface receptor *C3ar1* in labyrinthine macrophages may indicate enhanced macrophage migration signals (Figure 5H).[61]

In summary, our findings suggest that delayed glycogen breakdown, along with the abnormal accumulation and activation of macrophages in the labyrinth of dysfunctional placentas, could play a role in the pregnancy complications observed in perinatal lethal mice.

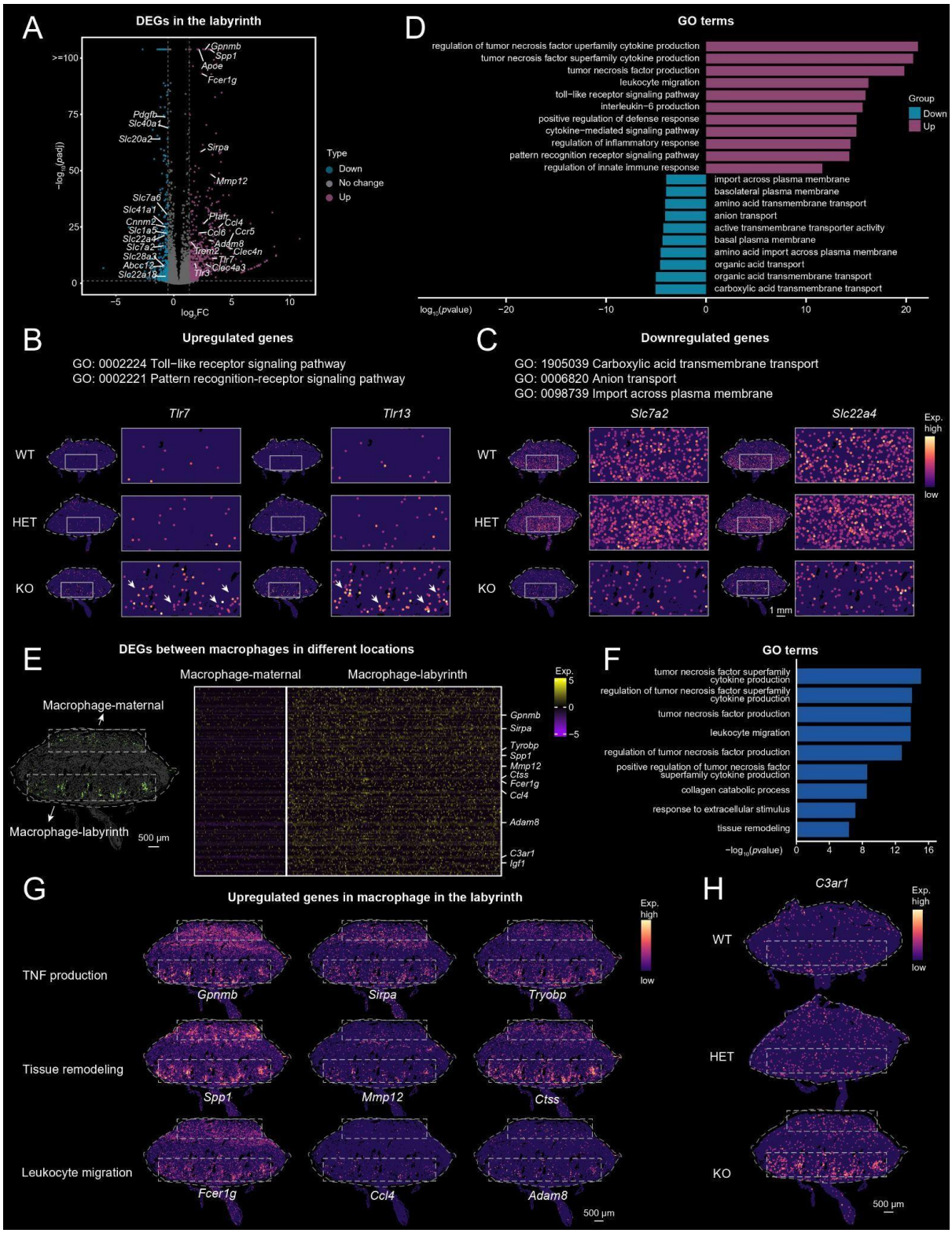
A
DEGs in the labyrinth
Gpnmb
Spp1
Apoe
Fcer1g
Pdgfb
Slc40a1
Slc20a2
Sirpa
Mmp12
Slc7a6
Slc41a1
Cnnm2
Slc1a5
Slc22a4
Slc7a2
Slc28a3
Abcc13
Slc22a18
Ptafr
Ccl4
Ccl6
Ccr5
Adam8
Trem2
Clec4n
Tlr7
Clec4a3
Tlr3
Type
Down
No change
Up
D
GO terms
regulation of tumor necrosis factor uperfamily cytokine production
tumor necrosis factor superfamily cytokine production
tumor necrosis factor production
leukocyte migration
toll−like receptor signaling pathway
interleukin−6 production
positive regulation of defense response
cytokine−mediated signaling pathway
regulation of inflammatory response
pattern recognition receptor signaling pathway
regulation of innate immune response
import across plasma membrane
basolateral plasma membrane
amino acid transmembrane transport
anion transport
active transmembrane transporter activity
basal plasma membrane
amino acid import across plasma membrane
organic acid transport
organic acid transmembrane transport
carboxylic acid transmembrane transport
Group
Down
Up
B
Upregulated genes
GO: 0002224 Toll−like receptor signaling pathway
GO: 0002221 Pattern recognition-receptor signaling pathway
Tlr7
Tlr13
WT
HET
KO
C
Downregulated genes
GO: 1905039 Carboxylic acid transmembrane transport
GO: 0006820 Anion transport
GO: 0098739 Import across plasma membrane
Slc7a2
Slc22a4
Exp.
high
low
1 mm
E
DEGs between macrophages in different locations
Macrophage-maternal
Macrophage-labyrinth
500 µm
Gpnmb
Sirpa
Tyrobp
Spp1
Mmp12
Ctss
Fcer1g
Ccl4
Adam8
C3ar1
Igf1
F
GO terms
tumor necrosis factor superfamily cytokine production
regulation of tumor necrosis factor superfamily cytokine production
tumor necrosis factor production
leukocyte migration
regulation of tumor necrosis factor production
positive regulation of tumor necrosis factor superfamily cytokine production
collagen catabolic process
response to extracellular stimulus
tissue remodeling
G
Upregulated genes in macrophage in the labyrinth
TNF production
Tissue remodeling
Leukocyte migration
Gpnmb
Sirpa
Tryobp
Spp1
Mmp12
Ctss
Fcer1g
Ccl4
Adam8
500 µm
H
C3ar1
WT
HET
KO
500 µm

Figure 5. Spatially disordered macrophages are correlated with immune activation and tissue repair in the defective placenta

(A) Volcano plot showing the differentially expressed genes (DEGs) in the labyrinth of KO placentas compared with WT placentas.
(B) Spatial visualization of representative upregulated genes in enriched GO terms on the WT, HET and KO placental sections.
(C) Spatial visualization of representative downregulated genes in enriched GO terms in the WT, HET and KO placenta sections.
(D) Two-sided bar plot showing the enriched GO terms of differentially upregulated and downregulated genes in the labyrinth of KO placentas.
(E) Heatmap showing the upregulated genes in macrophages within the labyrinth of KO placenta compared with macrophages within the maternal region.
(F) Bar plot showing the enriched GO terms of differentially upregulated genes in macrophages within the labyrinth of KO placentas.
(G) Spatial visualization of representative genes in enriched GO terms in the KO placenta section.
(H) Spatial visualization of *C3ar1* in the WT, HET and KO placenta sections.

Discussion

Identifying genes essential for normal placental development is crucial for understanding the molecular framework governing this process. This knowledge is instrumental in uncovering the genetic causes of placental developmental defects during pregnancy, which can have significant health implications. Here, we present a systematic effort to identify potential genes contributing to embryonic lethality through trajectory analysis and to assess placental defects in mouse mutants from a spatial cellular and molecular perspective. By generating the Spatiotemporal Transcriptomic Atlas of the Mouse Placenta (STAMP) spanning E9.5 to E18.5, we aim to unravel the mechanisms of embryonic lethality by examining spatial cellular and molecular changes in defective placentas.

Previous efforts to evaluate placental abnormalities in mouse mutants have primarily relied on morphological assessments using techniques such as *in situ* hybridization and immunohistochemistry staining.[10,62] However, these approaches often lack detailed cellular and molecular information. Our spatiotemporal atlas offers spatially resolved insights into

cellular dynamics and gene expression patterns during placental development, enabling us to identify affected cell types in the placenta and pinpoint the specific timing of emerging developmental abnormalities. Moreover, the spatially resolved transcriptome of defective placentas provides insights into the underlying mechanisms of embryonic lethality.

Furthermore, our work offers insights for optimizing culture conditions, facilitating the long-term development of mouse embryos outside the uterine environment. By removing the uterine barrier, researchers can directly investigate post-implantation morphogenesis and artificial embryogenesis in mammals. However, current *ex utero* systems face limitations in supporting embryos beyond the hindlimb formation stage (E11) due to insufficient oxygenation and nutrient supply, highlighting the critical role of the placenta.[14] Understanding the establishment of glycogen trophoblast cells function informs strategies such as supplementing glucose in culture media, essential for long-term culture.

In conclusion, our maps aid in unraveling the mechanisms of embryonic lethality by analyzing spatial cellular and molecular changes in defective placentas. This dataset serves as a valuable foundation for further investigations into placental development in both physiological and diseased contexts.

ACKNOWLEDGMENTS

The authors thank all members of the Liu Lab for their constructive advice and comments on the study. We are grateful to the Imaging Platform at Westlake University for the use of microscopes and to the Histochemical Platform for providing technological support in tissue handling. We would like to thank the Microscopy Core Facility (MCF) of Westlake University for our electron microscopy work and the technical assistance from Yilin Sun and Guicun Fang. We also thank the Laboratory Animal Research Center (LARC) at Westlake University for animal care and operational assistance. Furthermore, we would like to thank CHI BIOTECH CO., LTD. for single nuclei RNA sequencing support. This work was supported by the National Natural Science Foundation of China (32370784, 22DAA01467), the National Key R&D Program of China (2022YFA1105700, 2022YFC3400400) and the Westlake Education Foundation. Additionally, we thank the China National GeneBank for providing sequencing services for this project.

AUTHOR CONTRIBUTIONS

X.L. conceived the project. X.W., L.L. and X.L. supervised the project. Y.F., S.J., performed all experiments and prepared samples for Stereo-seq and snRNA-seq with help from Y.M., Y.Y., S.W., and X.L. Y.F., X.Z., Y.L. analyzed the data with support from Y.J. and T.X. C.Y. and S.S. performed the RIBOmap experiment. Y.F., J.T., Y.Y., W.P., S.C., L.T., X.W., L.L., and X.L. wrote and revised the manuscript with input from all authors.

DECLARATION OF INTERESTS

X.L. is a co-founder of iCamuno Biotherapeutics Ltd. The other authors declare no competing interests.

Tables with titles and legends

Table 1. All lethal mouse knockout lines according to previous reports, related to Figure 3

All genes are categorized according to the time of lethality. They are roughly divided into postnatal lethality and lethality at various stages of embryonic development. The table also provides information on whether placental phenotype defects have been reported, along with the corresponding references. Lethal, no homozygotes are recovered. Subviable, homozygotes recovered but at less or equal to 13% (≤13%). Viable, homozygotes recovered more than 13% (>13%).

Data and code availability

- The data that support the findings of this study have been deposited into CNGB Sequence Archive (CNSA) of China National GeneBank DataBase (CNGBdb) with accession number CNP0004934. The snRNA-seq data and Stereo-seq data are accessible on our interactive data portal at CNSA https://db.cngb.org/stomics/stamp/.

- All the code in this study can be found in the GitHub repository: https://github.com/xdliulab/Placenta_Project.

EXPERIMENTAL MODEL AND STUDY PARTICIPANT DETAILS

Animals

All strains of mice concerned in the study were in the C57BL/6J genetic background. The *Ano6*$^{+/-}$ mouse was generated by Cyagen Biosciences. The *Ano6* mouse mating strategy was crossing heterozygous male mice with heterozygous female mice in order to generate wildtype, heterozygous and homozygous offspring. All animal experiments were carried out with permission of the ethics committee on laboratory animal welfare of Westlake University (AP#22-032-2-LXD-7). All mice were housed in an SPF facility under a 12/12 hours light/dark cycle. Animals were mated at 16:00–17:00, and the vaginal plugs were checked by visual inspection the next morning (8:00–9:00).

METHOD DETAILS

Placenta dissection

Pregnant mice were euthanized, and their placentas were quickly dissected from the uterus. Cold DPBS was used to wash the placentas three times to remove blood. Yolk sac DNA was extracted to confirm genotypes (Vazyme, PD101-01). Surface water was carefully wiped away before the tissue was embedded in OCT (SAKURA, 4583), ensuring that air bubbles were avoided. The frozen blocks were then stored at -80°C. For paraffin embedding, the placentas were fixed overnight in 4% PFA at 4°C, dehydrated through a series of ethanol washes, cleaned three times in xylene, and finally embedded in paraffin (Leica, 39601006) overnight.

Stereo-seq experiment

Frozen sections with a thickness of 10 μm were attached to the surface of a 1 cm x 1 cm stereo-seq chip. The tissues were fixed with pre-chilled methanol at -20°C for 30 minutes, then stained with Qubit ssDNA (Invitrogen, Q10212). Tissue permeabilization was performed using STOmics PR Enzyme (1000028500) for 5 minutes. Reverse transcription was conducted at 42°C using the STOmics Gene Expression kit. Bead-purified cDNA was then amplified by PCR, followed by another round of bead purification. For library construction, the cDNA was

fragmented and amplified. The products were subsequently filtered twice, first with 0.6X and then with 0.2X beads.

Nuclei extraction and snRNA-seq

We prepared 200 mg of frozen tissue and transferred it into a 1.5 ml microcentrifuge tube, taking care not to thaw the tissue before lysis. We added 300 µl of NP40 lysis buffer, minced the tissue using scissors, then added an additional 1 ml of NP40 lysis buffer. We incubated the mixture on ice for 5-8 minutes to allow for lysis. After lysis, the suspension was passed through a 30 µm filter into a 5 ml tube and centrifuged at 4°C at 500 g for 5 minutes. Next, we added 1 ml of PBS containing 1% BSA and 1 U/µl RNase inhibitor, mixed gently by pipetting, and conducted microscopic quality checks. We assessed the integrity of the nuclear membrane and background using Trypan blue under a microscope and applied AOPI stain to evaluate nuclear concentration, viability, and aggregation of nuclei. After confirming satisfactory quality, we proceeded with labeling for downstream analysis as soon as possible.

Tissue sectioning

All frozen blocks were equilibrated in the box for at least 30 minutes before sectioning. The frozen embedded tissue was sectioned sagittally until reaching the umbilical cord, with each section being 10 µm thick. Paraffin-embedded sections were cut at a thickness of 5 µm. For the histological examination of the placenta, at least three sections, positioned 70 µm apart, were analyzed per placenta.

Hematoxylin-Eosin (H&E) staining

Frozen slices were allowed to recover for 20 minutes at room temperature before being fixed in 4% PFA for 3 minutes. Tissue sections were stained with hematoxylin for 6 minutes and with eosin for 2 minutes. Dehydration was carried out through an alcohol gradient of 75%, 85%, 95%, and 100%, followed by two xylene washes, each lasting 1 minute. Paraffin slices were incubated in hematoxylin for 6 minutes, rinsed in water, and then stained in eosin for 30 seconds.

Immunofluorescence staining

Placentas were dissected and post-fixed in 4% PFA/PBS for 30 minutes, then permeabilized in 0.1% Triton X-100/PBS for 30 minutes. Blocking was performed with 5% donkey serum and 1% BSA for 30 minutes at room temperature. Sections were incubated with diluted primary antibodies overnight at 4°C, washed three times with PBS, and then incubated with secondary antibodies for 1 hour at room temperature. Primary and secondary antibodies were used at the following concentrations: chicken anti-rat MCT1 (sigma, AB 1286-1, 1:200), rabbit anti-rat

MCT4 (Millipore, AB3314P, 1:100), rat anti-mouse CD31 (BD Pharmingen, 557355, 1:200), rabbit anti-mouse F4/80 (CST, 30325, 1:200), rabbit anti-mouse F4/80 (HUABIO, HA721520, 1:100), goat anti-rabbit IgG H&L (Abcam, Alexa Fluor 488, 1:500), goat anti-chicken IgY H&L (Abcam, Alexa Fluor 555, 1:500).

Periodic Acid–Schiff (PAS) staining

PAS staining was performed using a PAS staining kit (Cat #G1280, Solarbio) following the manufacturer's instructions. Paraffin sections were dewaxed to distilled water. The sections were treated with an oxidant for 10 minutes and subsequently rinsed in running tap water for 5 minutes. Samples were then stained with Schiff reagent for 15 minutes and rinsed again for 5 minutes. The sections were counterstained with Mayer's hematoxylin solution for 3 minutes. Following conventional dehydration and clearing in xylene, the sections were mounted with neutral gum. Quantification of the PAS-positive area relative to the total placental area for each section was performed using ImageJ software.

Quantitative PCR (qPCR)

Total RNA was extracted using the FastPure Cell/Tissue Total RNA Isolation Kit V2 (Vazyme RC112). Each RNA sample was reverse-transcribed with the GoScript Reverse Transcription system (A5001, Promega) using Oligo(dT) and random primers. Relative quantitation was determined using the BioRad CFX Touch and calculated by the comparative Ct method ($2^{-\Delta\Delta Ct}$), with the expression of β-Actin serving as the control.

Ribosome-bound mRNA mapping (RIBOmap)

10 μm thick placenta slices were mounted on confocal dishes. Tissues were fixed in 4% PFA for 15 minutes and permeabilized with cold methanol at -20°C for 1 hour. Yeast tRNAs were added to quench the tissues. Splint primers, padlock, and primer probes were added to the tissue and hybridized for 12 hours at 40°C. After washing twice in PBSTR and once with a high-salt washing buffer for 20 minutes each at 37°C, T4 ligase was added to the solution and incubated for 2 hours at room temperature. Rolling circle amplification of the DNA circle by phi29 polymerase was performed at 34°C for 30 minutes and at 30°C for 2 hours. Tissues were washed twice with 0.1% PBST. After incubation in modification solution for one hour at room temperature, tissues were monomerized with 4% acrylamide-0.2% bis-acrylamide for 15 minutes. Coverslips were then placed directly onto the polymerization solution and incubated under nitrogen flow for 1 hour, after which the coverslip was discarded. Tissues were digested in PK buffer mix (0.2 mg/ml PK final) for 1 hour at 37°C. Placentas were stripped for 10 minutes in 60% formamide twice. After 3 hours of incubation at room temperature, the fluorescent oligos were visualized by confocal fluorescence microscopy using LAS X software.

Transmission electron microscopy (TEM)

Placental tissues were rapidly collected and immersed in a solution of 2.5% glutaraldehyde and 2% paraformaldehyde in 0.1 M phosphate buffer (PB) at 4°C overnight for fixation. Post-fixation, the samples were washed three times with PB buffer and subsequently fixed with 2% osmium tetroxide for 60 minutes on ice. This was followed by a further fixation in 2% osmium tetroxide containing 2.5% potassium ferrocyanide for an additional 60 minutes on ice. The samples were dehydrated through a graded ethanol series (30%, 50%, 70%, 85%, 95%, and twice in 100%) for 10 minutes each step. They were then infiltrated and embedded in EPON12 resin. After sectioning into ultra thin slices (70 nm) and staining, the sections were imaged using a Thermo Fisher Talos 120 electron microscope operated at 80 kV. Quantification of glycogen granules per μm² in glycogen cells was performed using ImageJ software.

Placental glycogen content quantification

Whole placentas were immediately weighed on a scale. Each sample was treated with 0.5 mL of 30% KOH saturated with Na_2SO_4. The tubes were then placed in a boiling water bath for 30 minutes until a homogeneous solution formed. After removal from the bath, the tubes were cooled on ice. To precipitate the glycogen, 95% ethanol was added. The samples were left to stand on ice for 30 minutes, followed by centrifugation at 840 g for 30 minutes. The glycogen precipitates were dissolved in 3 mL of distilled water. To each mL of sample, 1 mL of 5% phenol solution was added, followed by the rapid addition of 5 mL of 98% H_2SO_4. The tubes were allowed to stand for 10 minutes, shaken, and then incubated at 30°C for 20 minutes. Blanks were prepared using 1 mL of distilled water. Absorbance was measured at 490 nm. Quantification of glycogen content and the percentage of glycogen weight relative to total placental weight were performed using GraphPad Prism software.

QUANTIFICATION AND STATISTICAL ANALYSIS

Data Processing of snRNA-seq Data

Single-nucleus RNA sequencing data processing utilized Cell Ranger (version 7.2.0, 10x Genomics) for quality control, alignment to the Mus musculus genome (refdata-gex-mm10-2020-A), and transcript quantification. The integration step employed the Cell Ranger aggr pipeline for sequencing depth normalization. Post-integration, cells with fewer than 500 genes detected or over 10% mitochondrial expression were excluded. The remaining data underwent normalization with Seurat's NormalizeData function (version 5.0.3).

Batch Correction and UMAP Nonlinear Dimensionality Reduction

The dataset underwent batch correction and dimensional reduction using IntegrateLayers with FastMNNIntegration. Neighborhood identification uses FindNeighbors (reduction = 'integrated.mnn', dims = 1:30), followed by cluster identification with FindClusters (resolution = seq(0.1, 0.2, 0.1)). Dimensional reduction concluded with RunUMAP (dims = 1:30, reduction = 'integrated.mnn'), visualizing cell clusters in two dimensions.

Identification of Differentially Expressed Genes

Differential gene expression was determined using FindMarkers, focusing on genes with only positive expression in specific clusters, detected in at least 25% of cells (min.pct = 0.25) and showing significant expression differences (logfc.threshold = 0.25).

SCENIC Analysis

Seurat objects converted to loom format enabled SCENIC analysis. GRNBoost2 from Arboreto inferred gene regulatory networks. The workflow involved runSCENIC_1_coexNetwork2modules, runSCENIC_2_createRegulons, and runSCENIC_3_scoreCells, assessing regulon activity across cell types with cisTarget databases set to mm10, and visualized through heatmaps.

Pseudotime Analyses and Characterization of GC Subtypes

Monocle 3 was used to transform Seurat objects into cell datasets and cluster cells (resolution = 1e-3). Trajectory analysis with learn_graph (use_partition = TRUE) identified developmental pathways, with order_cells setting the JZP cluster as the starting point. Visualization focused on pseudotime and cluster trajectories.

Cell-Cell Communication Analyses

Using CellChat, cell-cell communication networks were analyzed, utilizing the CellChatDB mouse database. IdentifyOverExpressedGenes and identifyOverExpressedInteractions pinpointed crucial genes and interactions. computeCommunProb (type = "triMean") and filterCommunication (min.cells = 10) refined the communication data.

Cell Type Integration

Data integration across sources standardized Seurat objects to the "RNA" assay using IntegrateLayers and "FastMNNIntegration". Neighborhoods were defined with FindNeighbors (dims = 1:30), and clusters identified with FindClusters. Visualization was achieved with RunUMAP, harmonizing and analyzing integrated datasets.

Ontology Annotation

GO enrichment analysis with clusterProfiler and org.Mm.eg.db mapped mouse genes to GO terms. Gene symbols converted to Entrez IDs with bitr preceded enrichGO analysis for clusters (snRNA-seq: pvalueCutoff = 0.01, pAdjustMethod = "fdr", minGSSize = 10, maxGSSize = 500, qvalueCutoff = 0.01 ; Stereo-seq: pvalueCutoff = 0.05, pAdjustMethod = "BH", minGSSize = 10, maxGSSize = 500, qvalueCutoff = 0.2).

Stereo-seq raw data processing

Single-end Stereo-seq fastq files were generated using a MGI DNBSEQ-Tx sequencer, which contained CID (coordinate identity), MID (molecular identity, UMI) and cDNA sequences. The retained reads were aligned to the mouse reference genome (mm10) (https://ftp.ensembl.org/pub/release-93/fasta/mus_musculus/dna/Mus_musculus.GRCm38.dna.primary_assembly.fa.gz) by STAR. Only mapped reads with a mapping quality score (MAPQ) > 10 were then annotated and calculated using handleBam (available at https://github.com/BGIResearch/handleBam). UMIs with identical CID and gene locus were collapsed, allowing 1 base pair of mismatch to correct for sequencing and PCR errors. Exonic reads were then used to construct an expression profile matrix comprising CIDs.

Image-based Cell Segmentation of Stereo-seq data

We utilized ssDNA staining image from the same section to segment cells by projecting the ssDNA staining image onto the Stereo-seq chip image. Firstly, a grayscale map was generated from the Stereo-seq data, with each pixel representing one DNB. Manual registration was conducted on both the grayscale map and the ssDNA staining image to align the pixels of the staining image with the DNB coordinates. Cell segmentation was then carried out using the scikit-image python package (v0.19.3).[63,64] Global threshold was used to filter the background noise of the registered image, and a mask was generated for segmentation. Gaussian-weighted local threshold was calculated to represent the position of the cell with block size of 45 and offset of 0.03. Cells with overlapped regions were segmented using the exact Euclidean distance transformation (with a minimal distance of 15). We then expanded the labels representing different cells in the label image by 5 pixels without causing overlaps, via expand_labels function. For each segmented cell, UMIs from all DNBs within the corresponding segmentation were aggregated per gene and subsequently summed to generate a cell-by-gene matrix for downstream analysis.

Spatially-constrained clustering of Stereo-seq data and region annotation

Cells with UMI counts below 200 (100 for E9.5, E15.5) were excluded from further analysis. The remaining raw count matrices of the placenta samples were normalized by SCTransform function in Seurat (v4.3.0).[65] Spatial information was taken into account for unsupervised clustering. The centroid of each cell was computed based on its spatial coordinates. The spatial k-nearest neighbor graph $G_{spatial}^{k1}$ ($k_1$is by default set to be 8) was constructed using Squidpy (v1.2.3).[66] This graph was then combined with the k-nearest neighbor graph $G_{expression}^{k2}$ based on transcriptomic data (k_2 is by default set to be 30). The combined graph $G_{combined} = G_{spatial}^{k1} \cup G_{expression}^{k2}$ was used as input for Leiden clustering. We annotated the placental region according to the anatomical structure, combined with spatially-constrained clustering and HE section partitioning.

Single cell level annotation of Stereo-seq data

Cells with UMI counts below 200 (100 for E9.5, E15.5) were excluded from further analysis. The remaining raw count data were normalized by the SCTransform function in Seurat (v4.3.0) to mitigate the effects of sequencing depth. Subsequently, high-quality single-nucleus RNA sequencing (snRNA-seq) data from the corresponding developmental stage were employed as a reference to annotate the Stereo-seq data using the TACCO (v0.3.0) framework.[27] Specifically, we mapped the Stereo-seq data using snRNA-seq data as a reference and the adjusted snRNA-seq data cell type proportions as the annotation prior distribution via the tacco.tools.annotate function. The annotation process assigned each spatial single cell the cell type with the highest score, indicating the most probable identity.

REFERENCES

1. Maltepe, E., and Fisher, S.J. (2015). Placenta: the forgotten organ. Annu. Rev. Cell Dev. Biol. *31*, 523–552.

2. Burton, G.J., and Fowden, A.L. (2015). The placenta: a multifaceted, transient organ. Philos. Trans. R. Soc. Lond. B Biol. Sci. *370*, 20140066.

3. Burton, G.J., and Jauniaux, E. (2015). What is the placenta? Am. J. Obstet. Gynecol. *213*, S6.e1, S6–S8.

4. Melchiorre, K., Giorgione, V., and Thilaganathan, B. (2022). The placenta and preeclampsia: villain or victim? Am. J. Obstet. Gynecol. *226*, S954–S962.

5. Burton, G.J., Fowden, A.L., and Thornburg, K.L. (2016). Placental Origins of Chronic Disease. Physiol. Rev. *96*, 1509–1565.

6. Walker, C.K., Krakowiak, P., Baker, A., Hansen, R.L., Ozonoff, S., and Hertz-Picciotto, I. (2015). Preeclampsia, placental insufficiency, and autism spectrum disorder or developmental delay. JAMA Pediatr. *169*, 154–162.

7. Hemberger, M., Hanna, C.W., and Dean, W. (2020). Mechanisms of early placental development in mouse and humans. Nat. Rev. Genet. *21*, 27–43.

8. Malassiné, A., Frendo, J.L., and Evain-Brion, D. (2003). A comparison of placental development and endocrine functions between the human and mouse model. Hum. Reprod. Update *9*, 531–539.

9. Adamson, S.L., Lu, Y., Whiteley, K.J., Holmyard, D., Hemberger, M., Pfarrer, C., and Cross, J.C. (2002). Interactions between trophoblast cells and the maternal and fetal circulation in the mouse placenta. Dev. Biol. *250*, 358–373.

10. Perez-Garcia, V., Fineberg, E., Wilson, R., Murray, A., Mazzeo, C.I., Tudor, C., Sienerth, A., White, J.K., Tuck, E., Ryder, E.J., et al. (2018). Placentation defects are highly prevalent in embryonic lethal mouse mutants. Nature *555*, 463–468.

11. Woods, L., Perez-Garcia, V., and Hemberger, M. (2018). Regulation of Placental Development and Its Impact on Fetal Growth-New Insights From Mouse Models. Front. Endocrinol. *9*, 570.

12. Elmore, S.A., Cochran, R.Z., Bolon, B., Lubeck, B., Mahler, B., Sabio, D., and Ward, J.M. (2022). Histology Atlas of the Developing Mouse Placenta. Toxicol. Pathol. *50*, 60–117.

13. Bolon, B. (2015). Pathology of the Developing Mouse: A Systematic Approach (CRC Press).

14. Aguilera-Castrejon, A., Oldak, B., Shani, T., Ghanem, N., Itzkovich, C., Slomovich, S., Tarazi, S., Bayerl, J., Chugaeva, V., Ayyash, M., et al. (2021). Ex utero mouse embryogenesis from pre-gastrulation to late organogenesis. Nature *593*, 119–124.

15. Tarazi, S., Aguilera-Castrejon, A., Joubran, C., Ghanem, N., Ashouokhi, S., Roncato, F., Wildschutz, E., Haddad, M., Oldak, B., Gomez-Cesar, E., et al. (2022). Post-gastrulation synthetic embryos generated ex utero from mouse naive ESCs. Cell *185*, 3290–3306.e25.

16. Radford, B.N., Zhao, X., Glazer, T., Eaton, M., Blackwell, D., Mohammad, S., Lo Vercio, L.D., Devine, J., Shalom-Barak, T., Hallgrimsson, B., et al. (2023). Defects in placental syncytiotrophoblast cells are a common cause of developmental heart disease. Nat. Commun. *14*, 1174.

17. Marsh, B., and Blelloch, R. (2020). Single nuclei RNA-seq of mouse placental labyrinth development. Elife *9*. 10.7554/eLife.60266.

18. Jiang, X., Wang, Y., Xiao, Z., Yan, L., Guo, S., Wang, Y., Wu, H., Zhao, X., Lu, X., and Wang, H. (2023). A differentiation roadmap of murine placentation at single-cell resolution. Cell Discov *9*, 30.

19. Moffitt, J.R., Lundberg, E., and Heyn, H. (2022). The emerging landscape of spatial profiling technologies. Nat. Rev. Genet. *23*, 741–759.

20. Bressan, D., Battistoni, G., and Hannon, G.J. (2023). The dawn of spatial omics.

Science *381*, eabq4964.

21. Vandereyken, K., Sifrim, A., Thienpont, B., and Voet, T. (2023). Methods and applications for single-cell and spatial multi-omics. Nat. Rev. Genet. *24*, 494–515.

22. You, Y., Fu, Y., Li, L., Zhang, Z., Jia, S., Lu, S., Ren, W., Liu, Y., Xu, Y., Liu, X., et al. (2023). Systematic comparison of sequencing-based spatial transcriptomic methods. bioRxiv, 2023.12.03.569744. 10.1101/2023.12.03.569744.

23. Chen, A., Liao, S., Cheng, M., Ma, K., Wu, L., Lai, Y., Qiu, X., Yang, J., Xu, J., Hao, S., et al. (2022). Spatiotemporal transcriptomic atlas of mouse organogenesis using DNA nanoball-patterned arrays. Cell *185*, 1777–1792.e21.

24. Yang, M., Ong, J., Meng, F., Zhang, F., Shen, H., Kitt, K., Liu, T., Tao, W., and Du, P. (2023). Spatiotemporal insight into early pregnancy governed by immune-featured stromal cells. Cell *186*, 4271–4288.e24.

25. Xu, Y., Zhao, J., Ren, Y., Wang, X., Lyu, Y., Xie, B., Sun, Y., Yuan, X., Liu, H., Yang, W., et al. (2022). Derivation of totipotent-like stem cells with blastocyst-like structure forming potential. Cell Res. *32*, 513–529.

26. Kalucka, J., de Rooij, L.P.M.H., Goveia, J., Rohlenova, K., Dumas, S.J., Meta, E., Conchinha, N.V., Taverna, F., Teuwen, L.-A., Veys, K., et al. (2020). Single-Cell Transcriptome Atlas of Murine Endothelial Cells. Cell *180*, 764–779.e20.

27. Mages, S., Moriel, N., Avraham-Davidi, I., Murray, E., Watter, J., Chen, F., Rozenblatt-Rosen, O., Klughammer, J., Regev, A., and Nitzan, M. (2023). TACCO unifies annotation transfer and decomposition of cell identities for single-cell and spatial omics. Nat. Biotechnol. *41*, 1465–1473.

28. Bouillot, S., Rampon, C., Tillet, E., and Huber, P. (2006). Tracing the glycogen cells with protocadherin 12 during mouse placenta development. Placenta *27*, 882–888.

29. Coan, P.M., Conroy, N., Burton, G.J., and Ferguson-Smith, A.C. (2006). Origin and characteristics of glycogen cells in the developing murine placenta. Dev. Dyn. *235*, 3280–3294.

30. Muccini, A.M., Tran, N.T., de Guingand, D.L., Philip, M., Della Gatta, P.A., Galinsky, R., Sherman, L.S., Kelleher, M.A., Palmer, K.R., Berry, M.J., et al. (2021). Creatine Metabolism in Female Reproduction, Pregnancy and Newborn Health. Nutrients *13*. 10.3390/nu13020490.

31. Outhwaite, J.E., Natale, B.V., Natale, D.R.C., and Simmons, D.G. (2015). Expression of aldehyde dehydrogenase family 1, member A3 in glycogen trophoblast cells of the murine placenta. Placenta *36*, 304–311.

32. Simmons, D.G., Rawn, S., Davies, A., Hughes, M., and Cross, J.C. (2008). Spatial and temporal expression of the 23 murine Prolactin/Placental Lactogen-related genes is not associated with their position in the locus. BMC Genomics *9*, 352.

33. Redline, R.W., Chernicky, C.L., Tan, H.Q., Ilan, J., and Ilan, J. (1993). Differential expression of insulin-like growth factor-II in specific regions of the late (post day 9.5) murine placenta. Mol. Reprod. Dev. *36*, 121–129.

34. Gasperowicz, M., Surmann-Schmitt, C., Hamada, Y., Otto, F., and Cross, J.C. (2013).

The transcriptional co-repressor TLE3 regulates development of trophoblast giant cells lining maternal blood spaces in the mouse placenta. Dev. Biol. *382*, 1–14.

35. Auman, H.J., Nottoli, T., Lakiza, O., Winger, Q., Donaldson, S., and Williams, T. (2002). Transcription factor AP-2gamma is essential in the extra-embryonic lineages for early postimplantation development. Development *129*, 2733–2747.

36. Kizaki, K., Satterfield, M.C., Hashizume, K., and Spencer, T. (2008). Trophoblast differentiation in the Ovine placenta: Insights into transcription factors and regulatory pathways. Biol. Reprod. *78*, 305–305.

37. Mould, A., Morgan, M.A.J., Li, L., Bikoff, E.K., and Robertson, E.J. (2012). Blimp1/Prdm1 governs terminal differentiation of endovascular trophoblast giant cells and defines multipotent progenitors in the developing placenta. Genes Dev. *26*, 2063–2074.

38. Renaud, S.J., Kubota, K., Rumi, M.A.K., and Soares, M.J. (2014). The FOS transcription factor family differentially controls trophoblast migration and invasion. J. Biol. Chem. *289*, 5025–5039.

39. Jin, S., Guerrero-Juarez, C.F., Zhang, L., Chang, I., Ramos, R., Kuan, C.-H., Myung, P., Plikus, M.V., and Nie, Q. (2021). Inference and analysis of cell-cell communication using CellChat. Nat. Commun. *12*, 1088.

40. Sharma, A., Lacko, L.A., Argueta, L.B., Glendinning, M.D., and Stuhlmann, H. (2019). miR-126 regulates glycogen trophoblast proliferation and DNA methylation in the murine placenta. Dev. Biol. *449*, 21–34.

41. Tunster, S.J., Watson, E.D., Fowden, A.L., and Burton, G.J. (2020). Placental glycogen stores and fetal growth: insights from genetic mouse models. Reproduction *159*, R213–R235.

42. Cao, J., Spielmann, M., Qiu, X., Huang, X., Ibrahim, D.M., Hill, A.J., Zhang, F., Mundlos, S., Christiansen, L., Steemers, F.J., et al. (2019). The single-cell transcriptional landscape of mammalian organogenesis. Nature *566*, 496–502.

43. Gulati, G.S., Sikandar, S.S., Wesche, D.J., Manjunath, A., Bharadwaj, A., Berger, M.J., Ilagan, F., Kuo, A.H., Hsieh, R.W., Cai, S., et al. (2020). Single-cell transcriptional diversity is a hallmark of developmental potential. Science *367*, 405–411.

44. Fung, C.W., Zhou, S., Zhu, H., Wei, X., Wu, Z., and Wu, A.R. (2022). Cell fate determining molecular switches and signaling pathways in Pax7-expressing somitic mesoderm. Cell Discov *8*, 61.

45. Zeng, H., Huang, J., Ren, J., Wang, C.K., Tang, Z., Zhou, H., Zhou, Y., Shi, H., Aditham, A., Sui, X., et al. (2023). Spatially resolved single-cell translatomics at molecular resolution. Science *380*, eadd3067.

46. Georgiades, P., Ferguson-Smith, A.C., and Burton, G.J. (2002). Comparative developmental anatomy of the murine and human definitive placentae. Placenta *23*, 3–19.

47. Zhang, Y., Le, T., Grabau, R., Mohseni, Z., Kim, H., Natale, D.R., Feng, L., Pan, H., and Yang, H. (2020). TMEM16F phospholipid scramblase mediates trophoblast fusion and placental development. Sci Adv *6*, eaba0310.

48. Takeda, K., Kaisho, T., and Akira, S. (2003). Toll-like receptors. Annu. Rev. Immunol. *21*, 335–376.

49. Zlotnik, A., and Yoshie, O. (2012). The chemokine superfamily revisited. Immunity *36*, 705–716.

50. Barclay, A.N., and Brown, M.H. (2006). The SIRP family of receptors and immune regulation. Nat. Rev. Immunol. *6*, 457–464.

51. Logtenberg, M.E.W., Scheeren, F.A., and Schumacher, T.N. (2020). The CD47-SIRPα Immune Checkpoint. Immunity *52*, 742–752.

52. Dobaczewski, M., Xia, Y., Bujak, M., Gonzalez-Quesada, C., and Frangogiannis, N.G. (2010). CCR5 signaling suppresses inflammation and reduces adverse remodeling of the infarcted heart, mediating recruitment of regulatory T cells. Am. J. Pathol. *176*, 2177–2187.

53. Chen, S., Saeed, A.F.U.H., Liu, Q., Jiang, Q., Xu, H., Xiao, G.G., Rao, L., and Duo, Y. (2023). Macrophages in immunoregulation and therapeutics. Signal Transduct Target Ther *8*, 207.

54. Travers, J.B., Rohan, J.G., and Sahu, R.P. (2021). New Insights Into the Pathologic Roles of the Platelet-Activating Factor System. Front. Endocrinol. *12*, 624132.

55. Deczkowska, A., Weiner, A., and Amit, I. (2020). The Physiology, Pathology, and Potential Therapeutic Applications of the TREM2 Signaling Pathway. Cell *181*, 1207–1217.

56. Liaw, L., Birk, D.E., Ballas, C.B., Whitsitt, J.S., Davidson, J.M., and Hogan, B.L. (1998). Altered wound healing in mice lacking a functional osteopontin gene (spp1). J. Clin. Invest. *101*, 1468–1478.

57. Freitas-Rodríguez, S., Folgueras, A.R., and López-Otín, C. (2017). The role of matrix metalloproteinases in aging: Tissue remodeling and beyond. Biochim. Biophys. Acta Mol. Cell Res. *1864*, 2015–2025.

58. Brown, R., Nath, S., Lora, A., Samaha, G., Elgamal, Z., Kaiser, R., Taggart, C., Weldon, S., and Geraghty, P. (2020). Cathepsin S: investigating an old player in lung disease pathogenesis, comorbidities, and potential therapeutics. Respir. Res. *21*, 111.

59. Saade, M., Araujo de Souza, G., Scavone, C., and Kinoshita, P.F. (2021). The Role of GPNMB in Inflammation. Front. Immunol. *12*, 674739.

60. van Duijn, A., Van der Burg, S.H., and Scheeren, F.A. (2022). CD47/SIRPα axis: bridging innate and adaptive immunity. J Immunother Cancer *10*. 10.1136/jitc-2022-004589.

61. Brennan, F.H., Jogia, T., Gillespie, E.R., Blomster, L.V., Li, X.X., Nowlan, B., Williams, G.M., Jacobson, E., Osborne, G.W., Meunier, F.A., et al. (2019). Complement receptor C3aR1 controls neutrophil mobilization following spinal cord injury through physiological antagonism of CXCR2. JCI Insight *4*. 10.1172/jci.insight.98254.

62. Mohun, T., Adams, D.J., Baldock, R., Bhattacharya, S., Copp, A.J., Hemberger, M., Houart, C., Hurles, M.E., Robertson, E., Smith, J.C., et al. (2013). Deciphering the Mechanisms of Developmental Disorders (DMDD): a new programme for phenotyping

embryonic lethal mice. Dis. Model. Mech. *6*, 562–566.

63. van der Walt, S., Schönberger, J.L., Nunez-Iglesias, J., Boulogne, F., Warner, J.D., Yager, N., Gouillart, E., Yu, T., and scikit-image contributors (2014). scikit-image: image processing in Python. PeerJ *2*, e453.

64. Neubert, P., and Protzel, P. (2014). Compact Watershed and Preemptive SLIC: On Improving Trade-offs of Superpixel Segmentation Algorithms. In 2014 22nd International Conference on Pattern Recognition (IEEE), pp. 996–1001.

65. Hao, Y., Hao, S., Andersen-Nissen, E., Mauck, W.M., 3rd, Zheng, S., Butler, A., Lee, M.J., Wilk, A.J., Darby, C., Zager, M., et al. (2021). Integrated analysis of multimodal single-cell data. Cell *184*, 3573–3587.e29.

66. Palla, G., Spitzer, H., Klein, M., Fischer, D., Schaar, A.C., Kuemmerle, L.B., Rybakov, S., Ibarra, I.L., Holmberg, O., Virshup, I., et al. (2022). Squidpy: a scalable framework for spatial omics analysis. Nat. Methods *19*, 171–178.

Supplemental figures

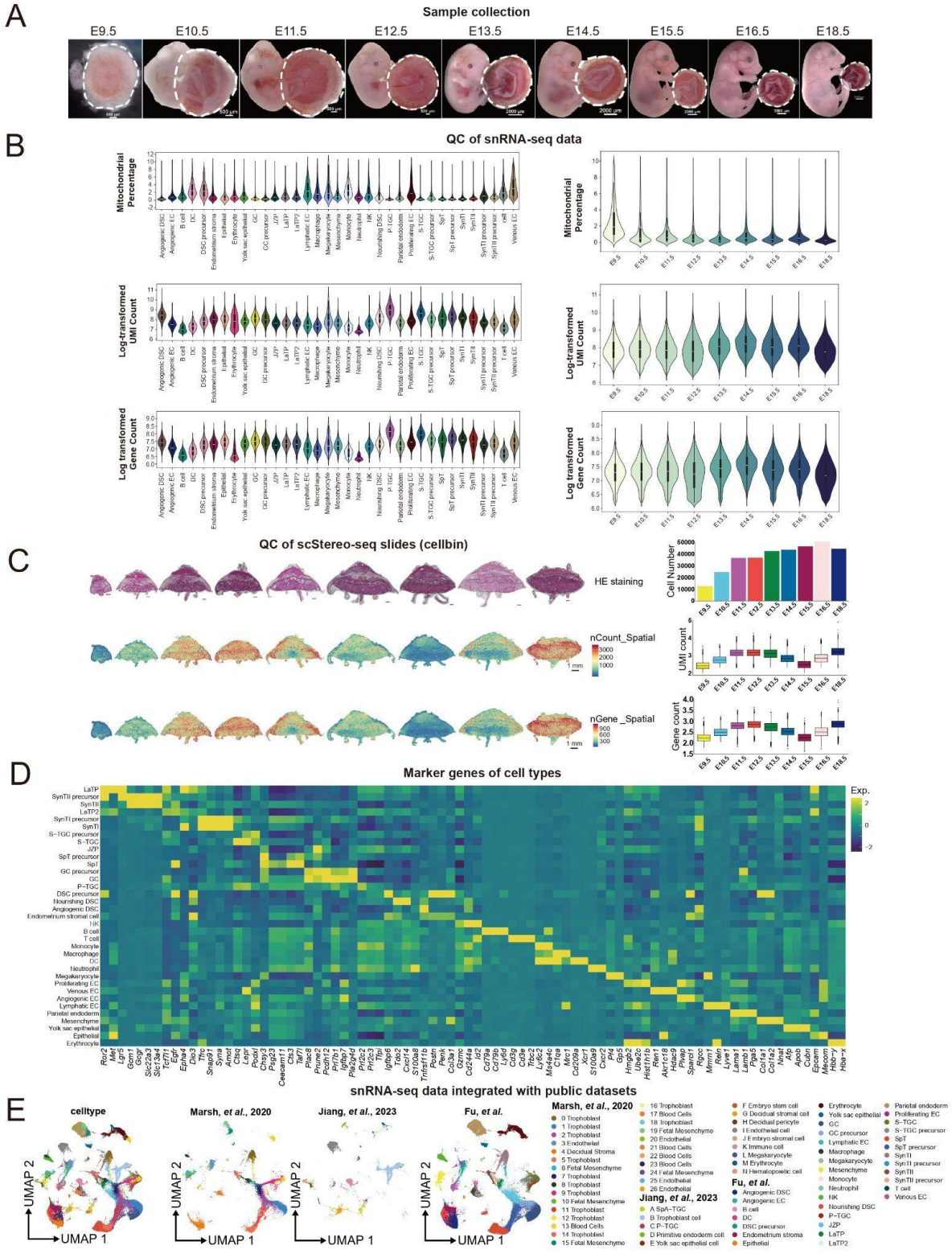

Figure S1. Experimental design and quality control analysis of snRNA-seq and Stereo-seq dataset, related to Figure 1

(A) Bright field images of samples from different developmental stages collected for sequencing experiments. White dashed lines indicate the collected placenta samples.

(B) Violin plots showing the number of reads and genes, and percentage of mitochondrial genes in the snRNA-seq data.

(C) Quality control of Stereo-seq data on cell number, UMI count and gene count. Representative hematoxylin and eosin (H&E) staining of the tissue section adjacent to the actual section used for Stereo-seq was shown. Stereo-seq spot overlay (cellbin) showing number of reads and genes. Scale bars, 500 μm.

(D) Heatmap showing top gene expression of all identified cell types.

(E) Integration of snRNA-seq data in this study with published datasets.[16,17]

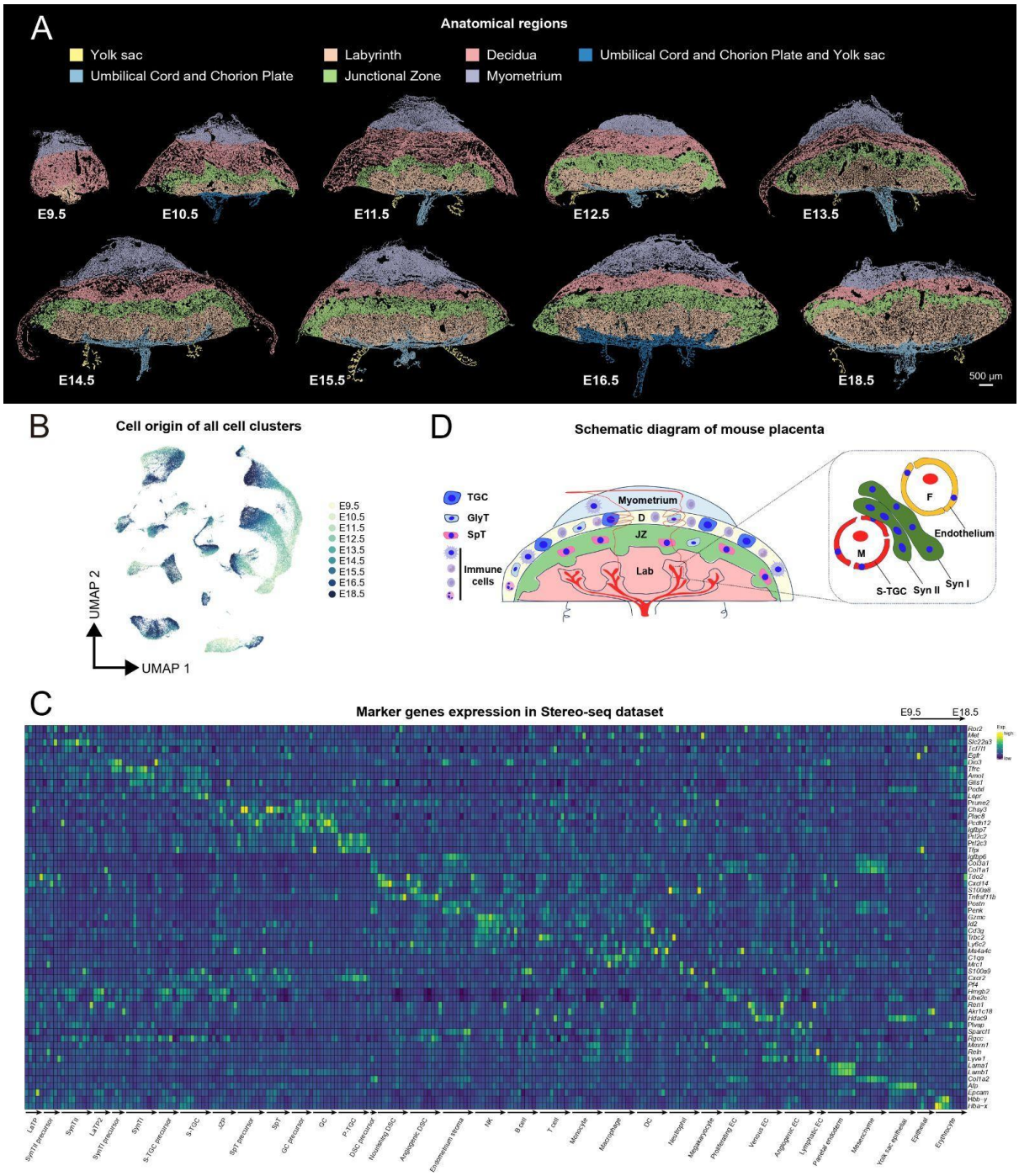
A
Anatomical regions
Yolk sac
Umbilical Cord and Chorion Plate
Labyrinth
Junctional Zone
Decidua
Myometrium
Umbilical Cord and Chorion Plate and Yolk sac
E9.5
E10.5
E11.5
E12.5
E13.5
E14.5
E15.5
E16.5
E18.5
500 μm
B
Cell origin of all cell clusters
E9.5
E10.5
E11.5
E12.5
E13.5
E14.5
E15.5
E16.5
E18.5
UMAP 2
UMAP 1
D
Schematic diagram of mouse placenta
TGC
GlyT
SpT
Immune cells
Myometrium
D
JZ
Lab
F
M
Endothelium
S-TGC
Syn II
Syn I
C
Marker genes expression in Stereo-seq dataset
E9.5
E18.5
LaTP
SynTII precursor
SynTII
LaTP2
SynTI precursor
SynTI
S-TGC precursor
S-TGC
JZP
SpT precursor
SpT
GC precursor
GC
P-TGC
DSC precursor
Nourishing DSC
Angiogenic DSC
Endometrium stroma
NK
B cell
T cell
Monocyte
Macrophage
DC
Neutrophil
Megakaryocyte
Proliferating EC
Venous EC
Angiogenic EC
Lymphatic EC
Parietal endoderm
Mesenchyme
Yolk sac epithelial
Epithelial
Erythrocyte

Figure S2. Anatomical regions and marker gene expression in Stereo-seq, related to Figure 1

(A) Anatomical regions were identified. Regions were colored based on anatomical region annotation. Scale bars, 500 μm.

(B) UMAP displaying snRNA-seq data from different time points.

(C) Heatmap showing marker gene expression of all identified cell types using Stereo-seq dataset.

(D) Schematic diagram of annotated placental regions based on our scStereto-seq data analysis.

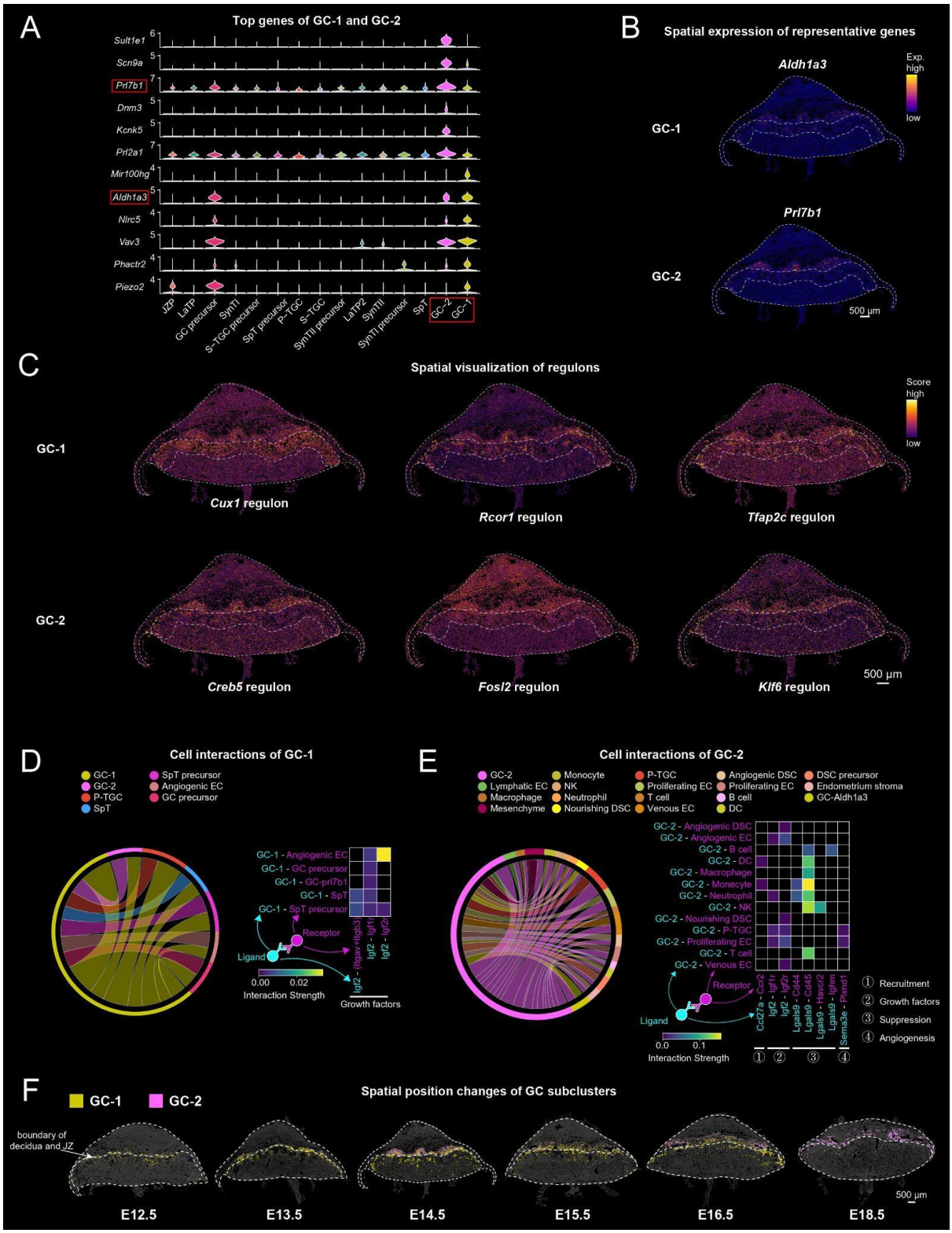
A
Top genes of GC-1 and GC-2
Sult1e1
Scn9a
Prl7b1
Dnm3
Kcnk5
Prl2a1
Mir100hg
Aldh1a3
Nlrc5
Vav3
Phactr2
Piezo2
JZP
LaTP
GC precursor
SynTI
S-TGC precursor
SpT precursor
P-TGC
S-TGC
SynTII precursor
LaTP2
SynTII
SynTI precursor
SpT
GC-2
GC-1
B
Spatial expression of representative genes
Aldh1a3
Exp.
high
low
GC-1
Prl7b1
GC-2
500 μm
C
Spatial visualization of regulons
Score
high
low
GC-1
Cux1 regulon
Rcor1 regulon
Tfap2c regulon
GC-2
Creb5 regulon
Fosl2 regulon
Klf6 regulon
500 μm
D
Cell interactions of GC-1
GC-1
GC-2
P-TGC
SpT
SpT precursor
Angiogenic EC
GC precursor
GC-1 - Angiogenic EC
GC-1 - GC precursor
GC-1 - GC-prl7b1
GC-1 - SpT
GC-1 - SpT precursor
Receptor
Ligand
Igf2 - Itgav+Itgb3
Igf2 - Igf1r
Igf2 - Igf2r
0.00
0.02
Interaction Strength
Growth factors
E
Cell interactions of GC-2
GC-2
Lymphatic EC
Macrophage
Mesenchyme
Monocyte
NK
Neutrophil
Nourishing DSC
P-TGC
Proliferating EC
T cell
Venous EC
Angiogenic DSC
Proliferating EC
B cell
DC
DSC precursor
Endometrium stroma
GC-Aldh1a3
GC-2 - Angiogenic DSC
GC-2 - Angiogenic EC
GC-2 - B cell
GC-2 - DC
GC-2 - Macrophage
GC-2 - Monecyte
GC-2 - Neutrophil
GC-2 - NK
GC-2 - Nourishing DSC
GC-2 - P-TGC
GC-2 - Proliferating EC
GC-2 - T cell
GC-2 - Venous EC
Receptor
Ligand
Ccl27a - Ccr2
Igf2 - Igf1r
Igf2 - Igf2r
Lgals9 - Cd44
Lgals9 - Cd45
Lgals9 - Havcr2
Lgals9 - Igfrn
Sema3e - Plxnd1
0.0
0.1
Interaction Strength
① Recruitment
② Growth factors
③ Suppression
④ Angiogenesis
F
GC-1
GC-2
Spatial position changes of GC subclusters
boundary of
decidua and JZ
500 μm
E12.5
E13.5
E14.5
E15.5
E16.5
E18.5

Figure S3. Molecular differences between two GC subclusters, related to Figure 2

(A) Violin plot showing top genes of GC-1 and GC-2 in all trophoblast cells.

(B) Spatial expression of top genes, *Aldh1a3* and *Prl7b1*, in GC-1 and GC-2 on an E14.5 placental section, respectively. Scale bars, 500 μm.

(C) Spatial visualization of selected regulons in GC-1 and GC-2 on E14.5 placental sections, respectively.

(D) Chord (left) diagram showing the interactions between GC-1 (sender) and other cell types (receiver). Heatmap (right) showing the selected ligand-receptor interactions.

(E) Chord (left) diagram showing the interactions between GC-2 (sender) and other cell types (receiver). Heatmap (right) showing the selected ligand-receptor interactions..

(F) The spatial visualization of the two GC subclusters from E12.5 to E18.5. Cells are colored by their annotation. Scale bars, 500 μm.

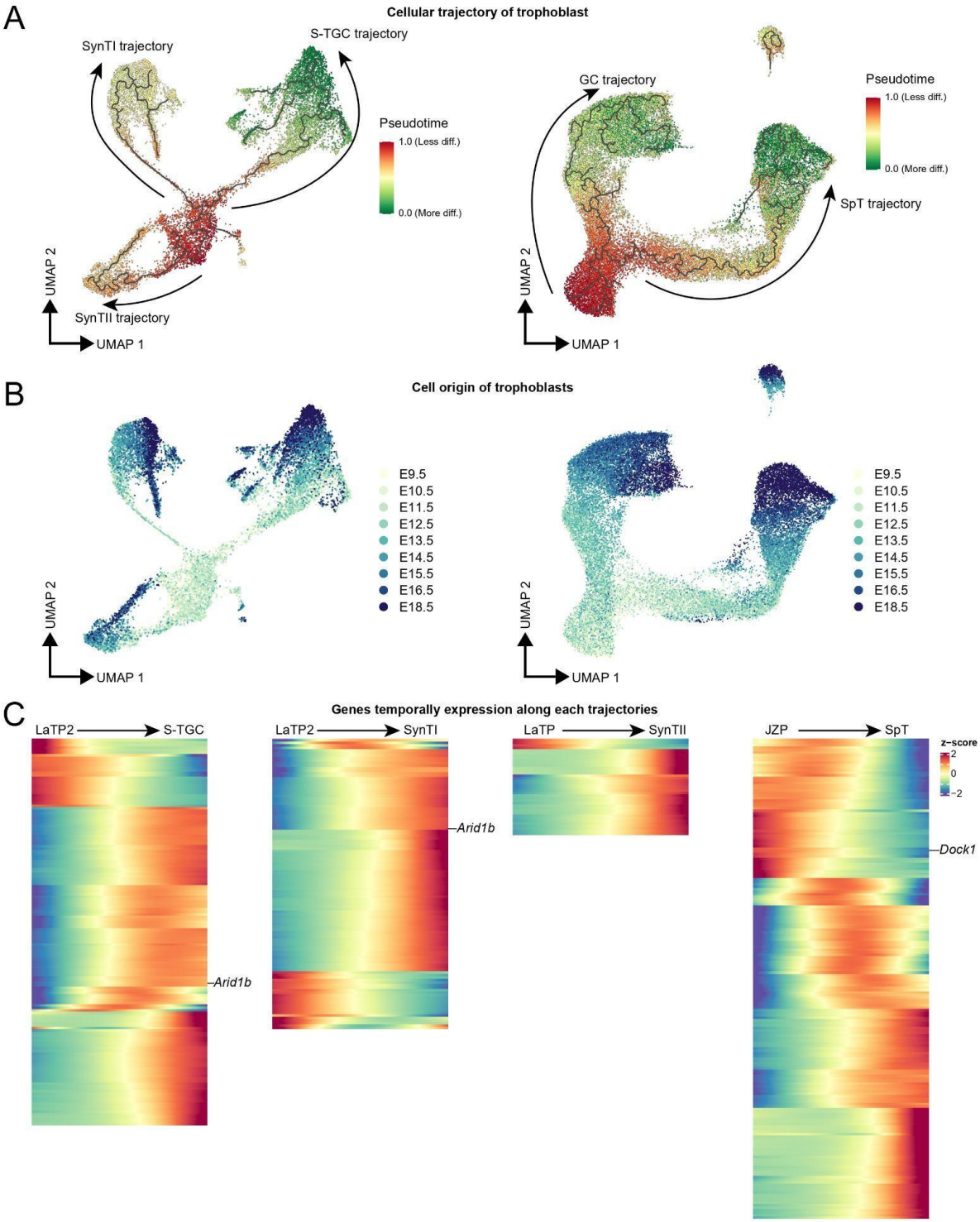
A
Cellular trajectory of trophoblast
SynTI trajectory
S-TGC trajectory
Pseudotime
1.0 (Less diff.)
0.0 (More diff.)
UMAP 2
SynTII trajectory
UMAP 1
GC trajectory
SpT trajectory
B
Cell origin of trophoblasts
E9.5
E10.5
E11.5
E12.5
E13.5
E14.5
E15.5
E16.5
E18.5
C
Genes temporally expression along each trajectories
LaTP2
S-TGC
SynTI
LaTP
SynTII
JZP
SpT
z-score
2
0
−2
Arid1b
Dock1

Figure S4. Cellular trajectory analysis reveals genes that may underlie placental defects, related to Figure 3

(A) Cellular trajectory reconstruction of trophoblast cells using the Monocle3[41] and CytoTRACE.[42]

(B) UMAP visualization showing the origin of trophoblasts based on the time point.

(C) Z-score heatmap of gene expression in different branches, where rows are genes and columns are cells ranked by pseudotime value. Genes were first fit with Moran's I test with ranked pseudotime as independent variable. Genes with the most significant time dependent model (*q*_value=0 and morans_I>0.25) were extracted and clustered hierarchical clustering. Cells were ordered according to scaled pseudotime value from 0 to 1.

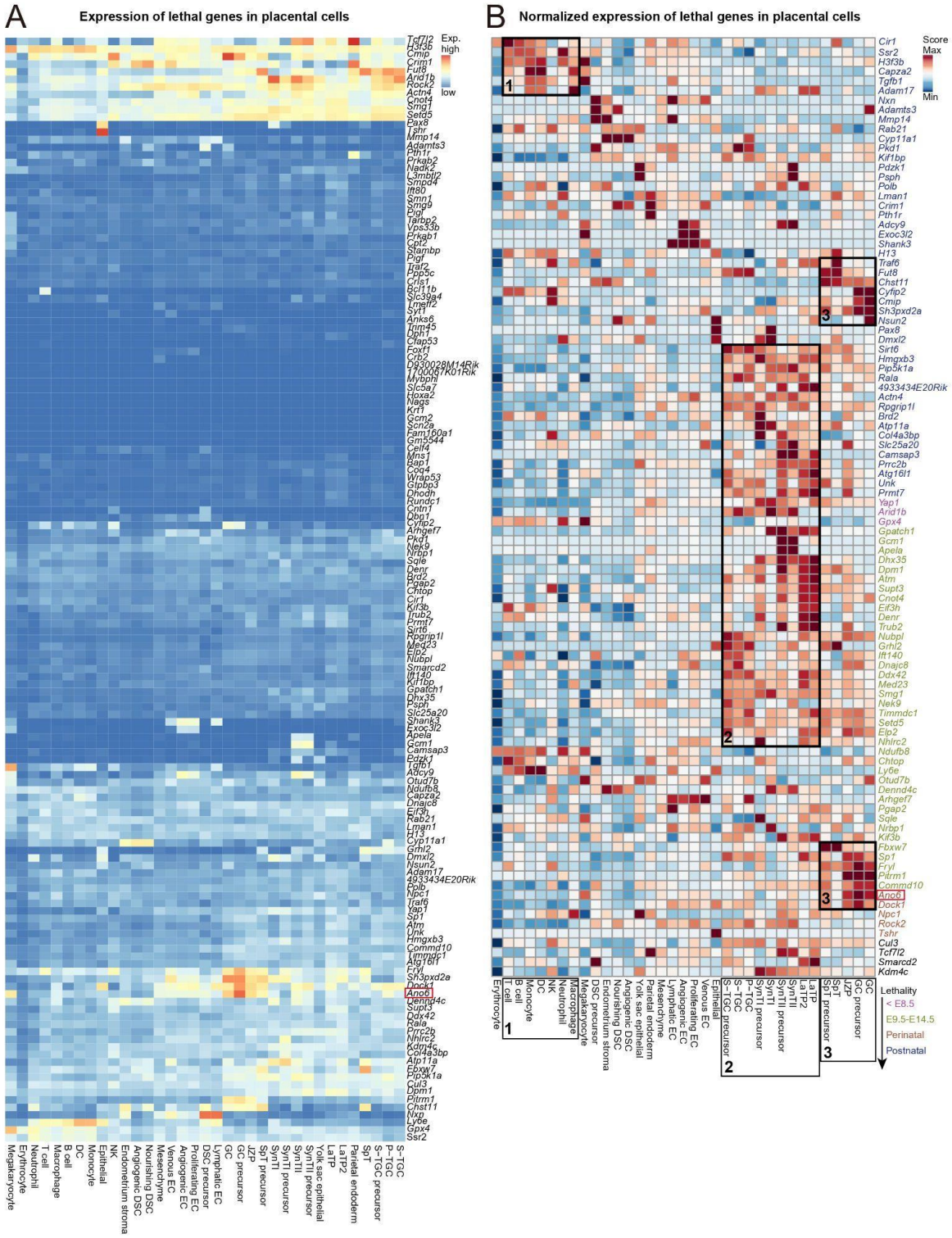
A
Expression of lethal genes in placental cells
Exp.
high
low
B
Normalized expression of lethal genes in placental cells
Score
Max
Min
Lethality
< E8.5
E9.5-E14.5
Perinatal
Postnatal

Figure S5. Expression pattern of embryonic lethal genes in placental cells, related to Figure 3

(A) Heatmap showing the expression patterns of 151 genes listed in Table 1 in annotated cell types across E9.5-18.5 placentas (snRNA-seq data). The *Ano6* gene is highlighted with a red box.

(B) Heatmap showing the normalized expression patterns of top 98 genes selected from Table 1 (based on the expression threshold) in annotated cell types across E9.5-18.5 placentas (snRNA-seq data). The mutant genes are colored with categories by the timing of lethality. The mutants represented in blue are postnatal lethal; the mutants represented in pink are lethal before E8.5; the mutants represented in green are lethal between E9.5-E14.5; the mutants represented in brown are perinatal lethal; and the mutants represented in black are lethal with uncertain embryonic stage. The boxes indicated selected enriched patterns, and the corresponding specific cell types of placenta are also encircled below. The *Ano6* gene is highlighted with a red box.

A

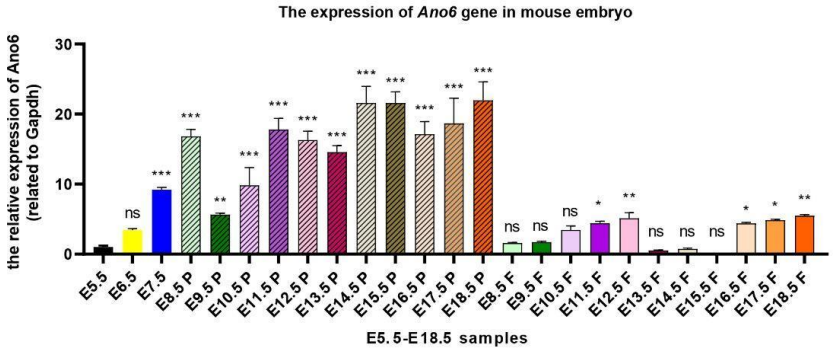

B

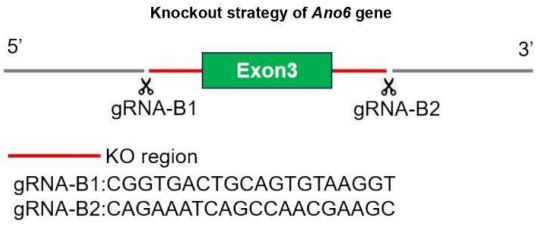

C

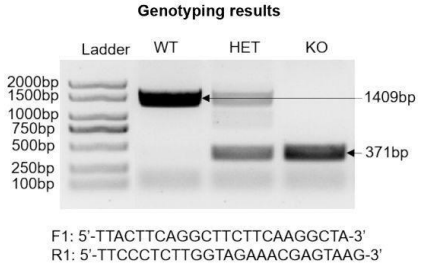

D

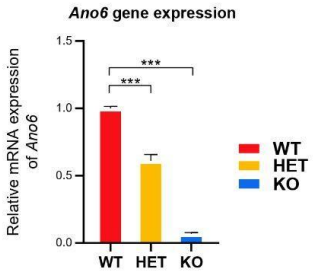

E

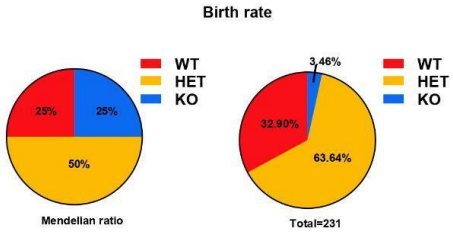

F

Birth statistics

Litter	#1	#2	#3	#4	#5	#6	#7	#8	#9	#10	#11	#12	#13	#14	#15	#16	#17	#18
Ano6 WT	3	2	3	0	2	2	3	2	1	0	5	4	3	1	8	1	2	2
Ano6 HET	5	5	5	5	6	4	3	3	4	3	2	3	8	6	3	1	3	5
Ano6 KO	0	0	1	0	0	0	0	0	0	0	0	1	0	2	0	0	0	0

Litter	#19	#20	#21	#22	#23	#24	#25	#26	#27	#28	#29	#30	#31	#32	#33	#34	#35	#36
Ano6 WT	2	2	2	2	2	3	2	1	2	1	3	1	1	0	5	0	2	1
Ano6 HET	5	3	3	6	4	4	3	5	4	3	3	4	4	8	2	4	5	3
Ano6 KO	0	2	1	0	0	0	1	0	0	0	0	0	0	0	0	0	0	0

Figure S6. *Ano6* knockout strategy and characterization of Ano6 KO mice, related to Figure 3

(A) The expression changes of *Ano6* gene in mouse embryos from E5.5 to E18.5 examined using quantitative PCR (qPCR), separately analyzing the expression in the fetal part and the placental part after E8.5. One-way analysis of variance (ANOVA). *$p < 0.05$, **$p < 0.01$, ***$p < 0.001$. All data represent means ± SEM.

(B) Strategy for knocking out the *Ano6* gene.

(C) Genotyping results of WT, HET and KO *Ano6* placentas.

(D) qPCR analysis of *Ano6* gene in WT/HET/KO placentas at E18.5. One-way analysis of variance (ANOVA). ***$p < 0.001$. All data represent means ± SEM.

(E) Birth rate statistics of *Ano6* gene knockout mice.

(F) Birth statistics of *Ano6* gene knockout mice.

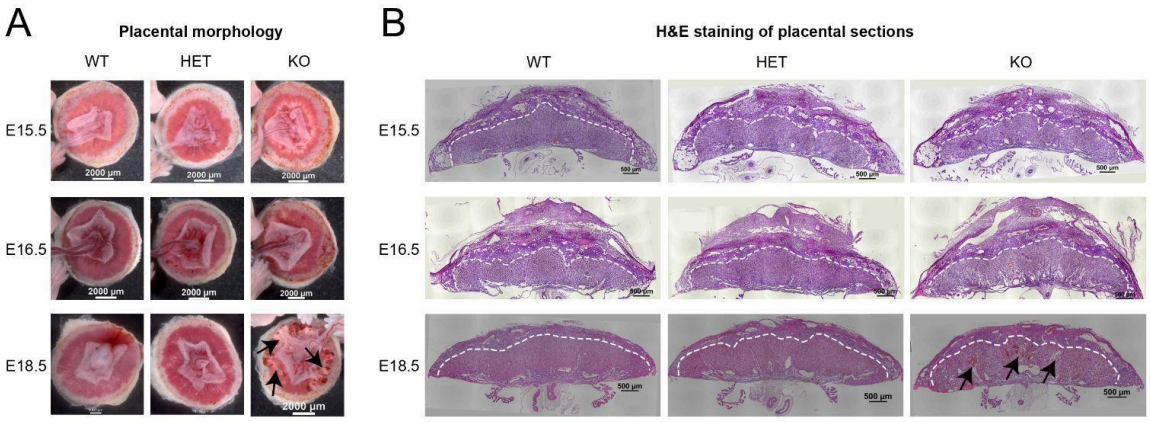

Figure S7. Morphological phenotypes of *Ano6* KO placentas, related to Figure 3

(A) Representative images of placentas from WT, HET, and KO mice at E15.5, E16.5, and E18.5. Black arrows point to the phenotypic defects in the KO placenta. Scale bars, 2000 μm. (B) H&E staining of WT, HET, and KO placental sections at E15.5, E16.5, and E18.5. The black arrow indicates the location where phenotypic abnormalities appear. Scale bars, 500 μm.

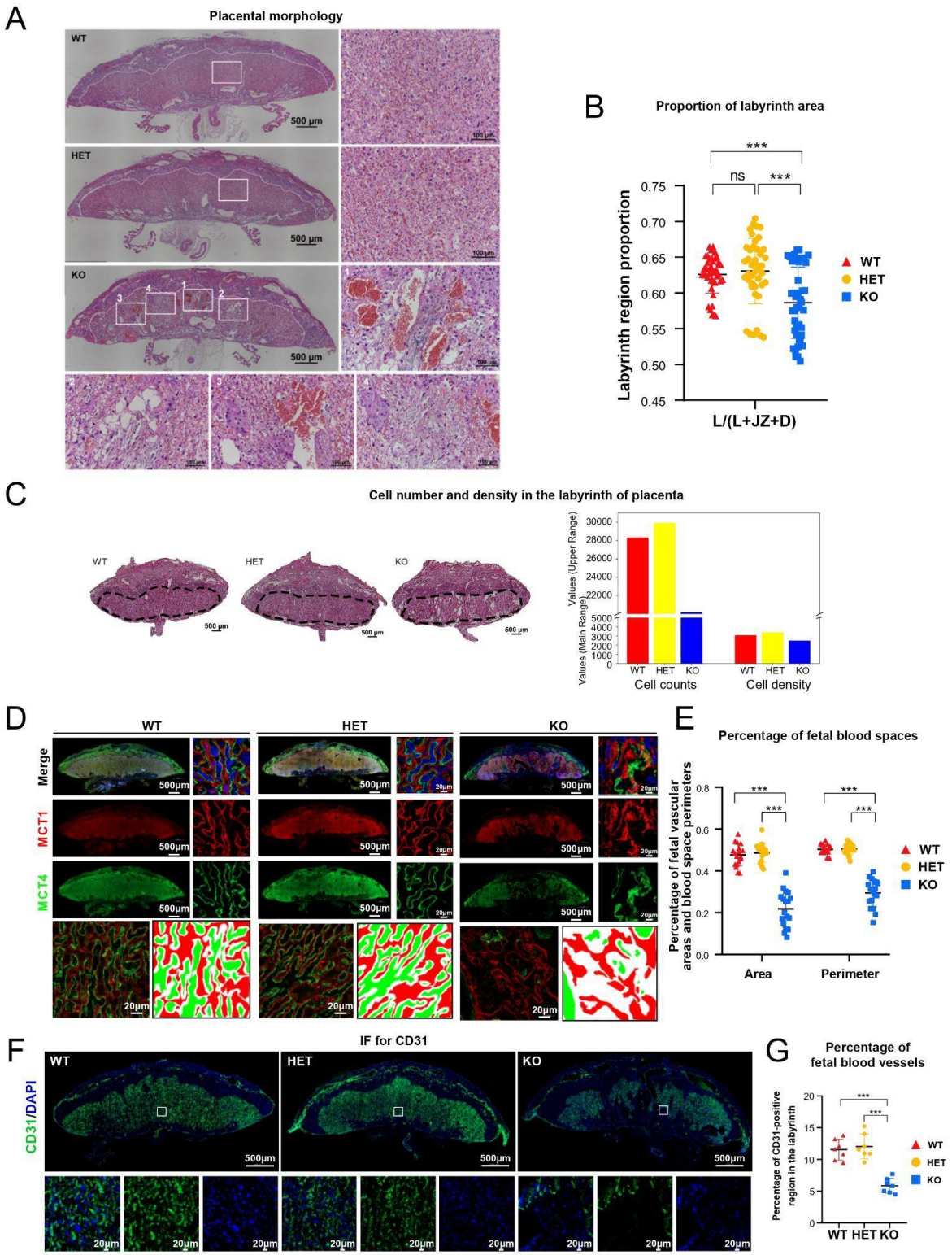
A
Placental morphology
WT
HET
KO
500 μm
B
Proportion of labyrinth area
Labyrinth region proportion
L/(L+JZ+D)
ns
***
WT
HET
KO
C
Cell number and density in the labyrinth of placenta
Values (Upper Range)
Values (Main Range)
Cell counts
Cell density
D
Merge
MCT1
MCT4
500μm
20μm
E
Percentage of fetal blood spaces
Percentage of fetal vascular areas and blood space perimeters
Area
Perimeter
F
IF for CD31
CD31/DAPI
G
Percentage of fetal blood vessels
Percentage of CD31-positive region in the labyrinth

Figure S8. *Ano6* knockout mice exhibit placenta developmental defects in the labyrinth layer, related to Figure 3

(A) H&E staining of WT/HET/KO placentas at E18.5. Scale bars, 500 μm (overall shape) and 100 μm (high-magnification view).

(B) Statistics on the proportion of the labyrinth region in total area of the placenta. One-way analysis of variance (ANOVA). ***$p < 0.001$. All data represent means ± SEM.

(C) H&E staining of WT/HET/KO placentas (left, the labyrinth region was encircled), and statistical results of cell quantity and cell density in the labyrinth region of WT, HET, and KO placentas (right). Scale bars, 500 μm.

(D) MCT1 and MCT4 immunofluorescence staining of the WT/HET/KO placentas at E18.5. MCT1 is specifically expressed in the SynTI layer that faces maternal blood sinuses, while MCT4 specifically stains the SynTII layer that encloses fetal blood vessels. Scale bars, 500 μm (overall shape) and 20 μm (high-magnification view).

(E) Percentage of fetal blood spaces as determined by MCT4-enclosed areas/(MCT1+MCT4)-enclosed areas (left). And percentage of MCT4-defined perimeters of the syncytial layers facing fetal blood vessels/(MCT1+MCT4)-defined perimeters (right). WT: n=18, HET: n=18, KO: n=18. Two-way analysis of variance (ANOVA). ***$p < 0.001$. All data represent means ± SEM.

(F) CD31 immunofluorescence staining of the WT/HET/KO placentas at E18.5. CD31 labels fetal blood vessels. Scale bars, 500 μm (overall shape) and 20 μm (high-magnification view).

(G) Percentage of fetal blood vessels in the labyrinth region. WT: n=7, HET: n=7, KO: n=7. One-way analysis of variance (ANOVA). ***$p < 0.001$. All data represent means ± SEM.

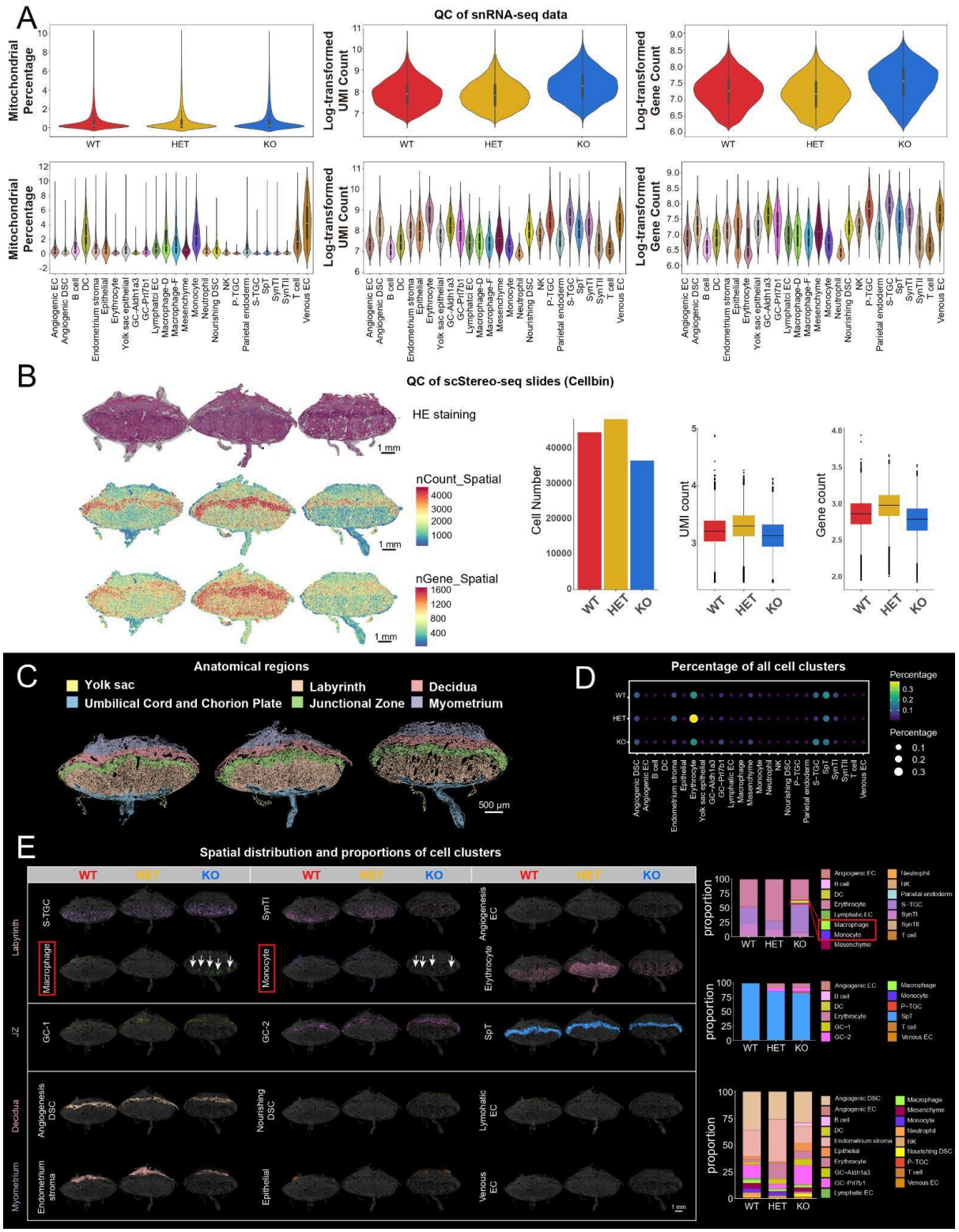
A
QC of snRNA-seq data
Mitochondrial Percentage
Log-transformed UMI Count
Log-transformed Gene Count
WT
HET
KO
Angiogenic EC
Angiogenic DSC
B cell
DC
Endometrium stroma
Epithelial
Erythrocyte
Yolk sac epithelial
GC-Aldh1a3
GC-Pri7b1
Lymphatic EC
Macrophage-D
Macrophage-F
Mesenchyme
Monocyte
Neutrophil
Nourishing DSC
NK
P-TGC
Parietal endoderm
S-TGC
SpT
SynTI
SynTII
T cell
Venous EC
B
QC of scStereo-seq slides (Cellbin)
HE staining
nCount_Spatial
nGene_Spatial
1 mm
Cell Number
UMI count
Gene count
C
Anatomical regions
Yolk sac
Umbilical Cord and Chorion Plate
Labyrinth
Junctional Zone
Decidua
Myometrium
500 μm
D
Percentage of all cell clusters
Percentage
E
Spatial distribution and proportions of cell clusters
Labyrinth
JZ
Decidua
Myometrium
S-TGC
Macrophage
SynTI
Monocyte
Angiogenesis EC
Erythrocyte
GC-1
GC-2
SpT
Angiogenesis DSC
Nourishing DSC
Lymphatic EC
Endometrium stroma
Epithelial
Venous EC
proportion

Figure S9. Experimental design and quality control analysis of snRNA-seq and Stereo-seq, related to Figure 3

(A) Violin plots showing the mitochondrial percentage, UMIs and genes in WT/HET/KO placentas (top) and in each cell type (bottom).

(B) Quality check of Stereo-seq data. H&E staining of the tissue slides adjacent to the tissue slides used for Stereo-seq. Stereo-seq spot overlay (cellbin) showing number of genes and reads. Scale bars, 500 μm.

(C) Identification of anatomical regions on WT/HET/KO placentas. Regions are colored based on anatomical region annotation. Scale bars, 500 μm.

(D) Bubble plot showing the percentage of all cell types in the E18.5 WT, HET, and KO placentas using Stereo-seq data.

(E) Cell type distribution in E18.5 WT, HET, and KO placenta sections. Differences in *Ano6* KO placenta compared with the WT/HET placentas are marked red. Cells were colored based on cell type annotation. Bar plots showing cell subcluster proportions in the corresponding regions. Scale bars, 500 μm.

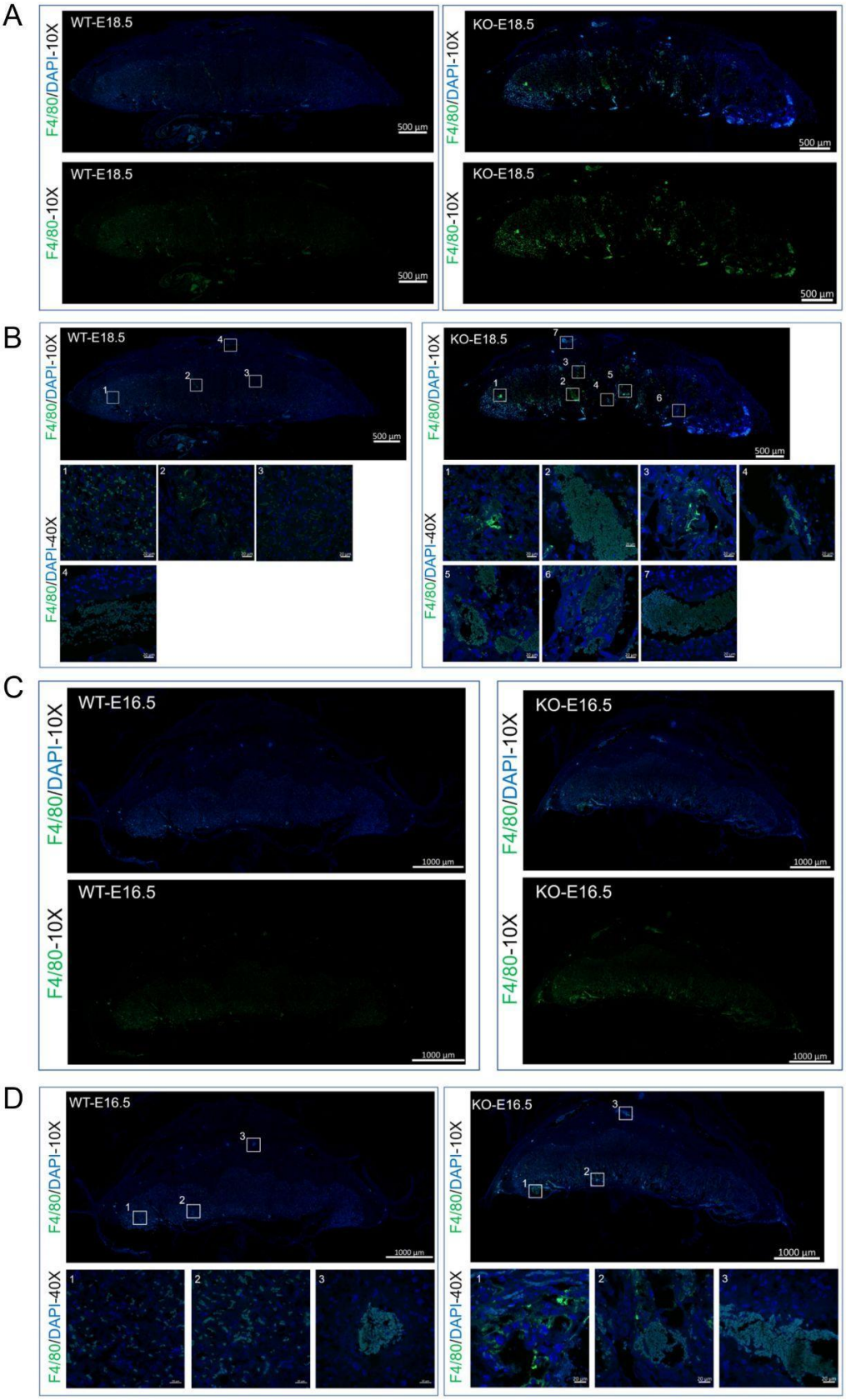
A
WT-E18.5
KO-E18.5
F4/80/DAPI-10X
F4/80-10X
500 µm
B
F4/80/DAPI-40X
C
WT-E16.5
KO-E16.5
1000 µm
D

Figure S10. The accumulation of macrophages in the labyrinth of KO placentas at E18.5, related to Figure 3

(A) F4/80 immunofluorescence staining of the WT and KO placentas at E18.5. F4/80 labels macrophages. Scale bars, 500 μm.

(B) F4/80 immunofluorescence staining of the WT and KO placentas at E18.5. F4/80 labels macrophages. Scale bars, 500 μm (overall shape) and 20 μm (high-magnification view).

(C) F4/80 immunofluorescence staining of the WT and KO placentas at E16.5. Scale bars, 500 μm.

(D) F4/80 immunofluorescence staining of the WT and KO placentas at E16.5. F4/80 labels macrophages. Scale bars, 500 μm (overall shape) and 20 μm (high-magnification view).

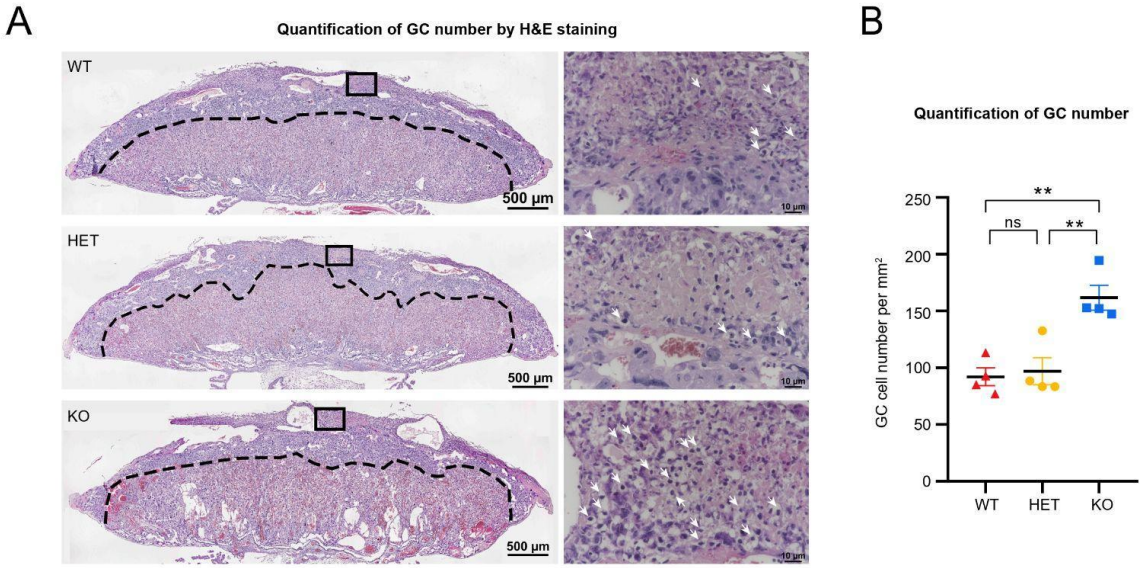

Figure S11. Quantification of glycogen cell number in KO placentas using hematoxylin and eosin (H&E) staining, related to Figure 4

(A) H&E staining of WT, HET and KO placentas. The black dashed line indicates the boundary between the JZ and decidua. The glycogen cells in JZ and decidua are characterized by vacuolated, glycogen-rich cytoplasm and appear as compact cell islets. Scale bars, 500 μm (overall shape) and 10 μm (high-magnification view).

(B) The glycogen cell number in JZ and decidua per mm^2. WT (n=4), HET (n=4), KO (n=4). One-way analysis of variance (ANOVA). $^{**}p < 0.01$. All data represent means ± SEM.

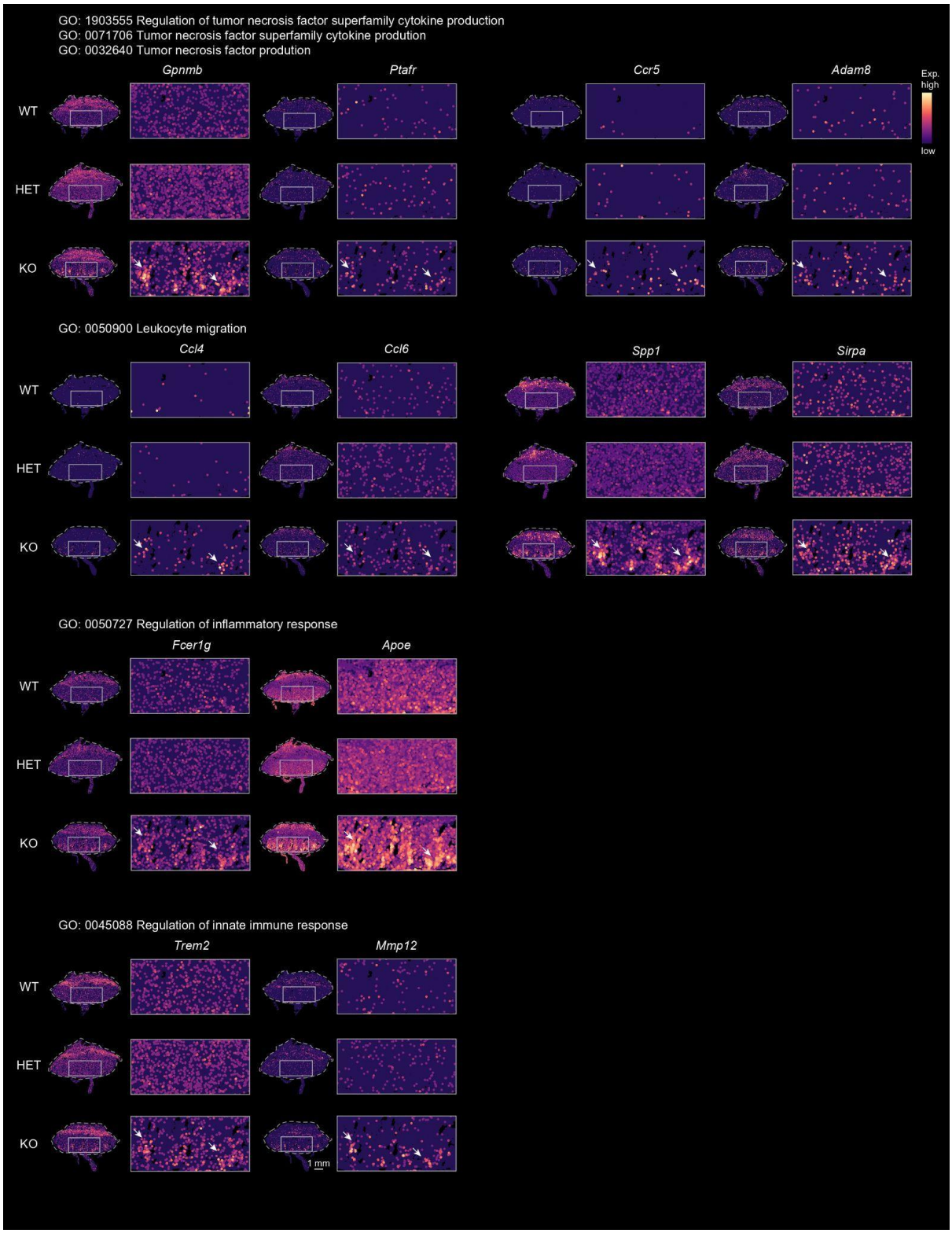
GO: 1903555 Regulation of tumor necrosis factor superfamily cytokine production
GO: 0071706 Tumor necrosis factor superfamily cytokine prodution
GO: 0032640 Tumor necrosis factor prodution
Gpnmb
Ptafr
Ccr5
Adam8
Exp.
high
low
WT
HET
KO
GO: 0050900 Leukocyte migration
Ccl4
Ccl6
Spp1
Sirpa
WT
HET
KO
GO: 0050727 Regulation of inflammatory response
Fcer1g
Apoe
WT
HET
KO
GO: 0045088 Regulation of innate immune response
Trem2
Mmp12
WT
HET
KO
1 mm

Figure S12. Spatial distribution of differentially expressed genes in the labyrinth between KO and WT placentas, related to Figure 5

Spatial visualization of representative upregulated genes in enriched GO terms on the WT, HET and KO placental sections.

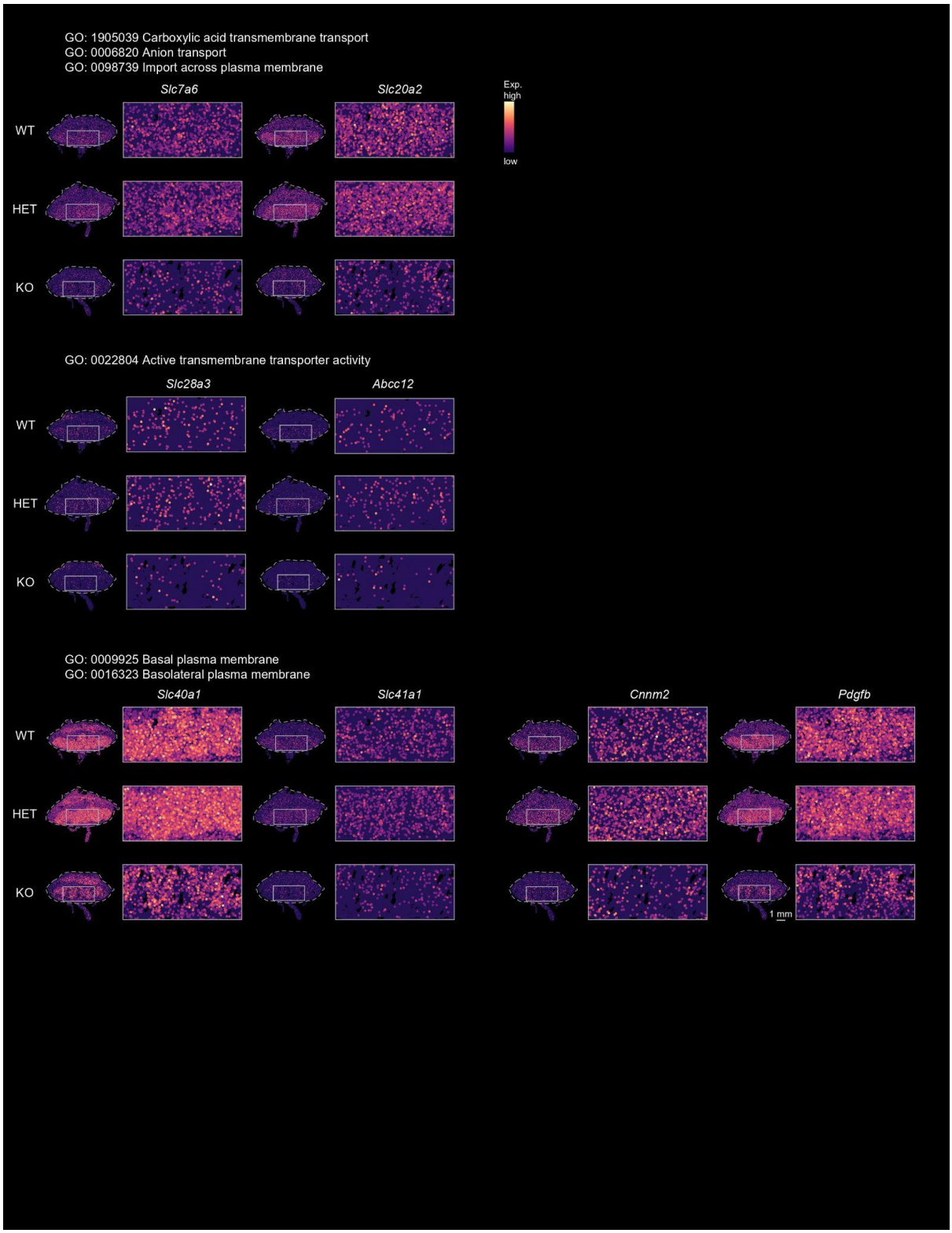
GO: 1905039 Carboxylic acid transmembrane transport
GO: 0006820 Anion transport
GO: 0098739 Import across plasma membrane
Slc7a6
Slc20a2
Exp.
high
low
WT
HET
KO
GO: 0022804 Active transmembrane transporter activity
Slc28a3
Abcc12
WT
HET
KO
GO: 0009925 Basal plasma membrane
GO: 0016323 Basolateral plasma membrane
Slc40a1
Slc41a1
Cnnm2
Pdgfb
WT
HET
KO
1 mm

Figure S13. Spatial distribution of differentially expressed genes in the labyrinth between KO and WT placentas, related to Figure 5

Spatial visualization of representative downregulated genes in enriched GO terms on the WT, HET and KO placental sections.